



Calhoun: The NPS Institutional Archive
DSpace Repository

Theses and Dissertations

1. Thesis and Dissertation Collection, all items

1978

Laser induced evaporation from stainless steel surfaces.

Hwang, Zen Wen

Monterey, California. Naval Postgraduate School

<http://hdl.handle.net/10945/18480>

Copyright is reserved by the copyright owner.

Downloaded from NPS Archive: Calhoun



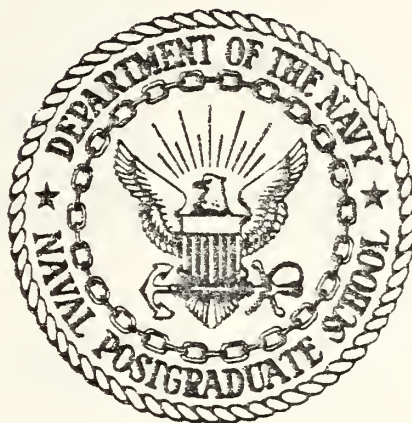
Calhoun is the Naval Postgraduate School's public access digital repository for research materials and institutional publications created by the NPS community. Calhoun is named for Professor of Mathematics Guy K. Calhoun, NPS's first appointed -- and published -- scholarly author.

Dudley Knox Library / Naval Postgraduate School
411 Dyer Road / 1 University Circle
Monterey, California USA 93943

<http://www.nps.edu/library>

NAVAL POSTGRADUATE SCHOOL

Monterey, California



THESIS

LASER INDUCED EVAPORATION FROM
STAINLESS STEEL SURFACES

by

Zen Wen Hwang

December 1978

Thesis Advisor:

F. Schwirzke

Approved for public release; distribution unlimited.

T187440

REPORT DOCUMENTATION PAGE		READ INSTRUCTIONS BEFORE COMPLETING FORM
1. REPORT NUMBER	2. GOVT ACCESSION NO.	3. RECIPIENT'S CATALOG NUMBER
4. TITLE (and Subtitle) Laser Induced Evaporation from Stainless Steel Surfaces		5. TYPE OF REPORT & PERIOD COVERED Master's Thesis; December 1978
		6. PERFORMING ORG. REPORT NUMBER
7. AUTHOR(s) Zen Wen Hwang		8. CONTRACT OR GRANT NUMBER(s)
9. PERFORMING ORGANIZATION NAME AND ADDRESS Naval Postgraduate School Monterey, California 93940		10. PROGRAM ELEMENT, PROJECT, TASK AREA & WORK UNIT NUMBERS
11. CONTROLLING OFFICE NAME AND ADDRESS Naval Postgraduate School Monterey, California 93940		12. REPORT DATE December 1978
		13. NUMBER OF PAGES 100
14. MONITORING AGENCY NAME & ADDRESS (if different from Controlling Office)		15. SECURITY CLASS. (of this report) Unclassified
		15a. DECLASSIFICATION/DOWNGRADING SCHEDULE
16. DISTRIBUTION STATEMENT (of this Report) Approved for public release; distribution unlimited.		
17. DISTRIBUTION STATEMENT (of the abstract entered in Block 20, if different from Report)		
18. SUPPLEMENTARY NOTES		
19. KEY WORDS (Continue on reverse side if necessary and identify by block number) Laser Induced Evaporation Laser-target damage mechanism		
20. ABSTRACT (Continue on reverse side if necessary and identify by block number) Laser-induced evaporation from a stainless steel surface was the laser-target damage mechanism which was studied. Infrared laser pulses with irradiances higher than 10^9 W/cm ² were produced by a Q-switched neodymium glass laser. Experiments were performed in a vacuum chamber evacuated to about 10^{-6} Torr. The mass of evaporated material, area of laser-drilled hole and depth of damaged hole were measured. Results showed that the mass of		

ABSTRACT (Cont'd)

evaporated material was proportional to $F^{1/2}$ where F is the laser flux in W/cm^2 . Surface damage phenomena were studied by metallographic methods using an optical microscope and scanning electron microscope (SEM). Evaporated materials were partially collected and analyzed separately with the SEM and Princeton Gamma Tech (PGT) 1000 x-ray analyzer. Results for 40 laser shots on one target showed the deposition of small pellets on the collector. The number of pellets depends on the number of laser shots. After 40 shots a pellet density of 10^8 particles/ cm^2 with an average particle separation of 10^{-4} cm was observed. The average particle diameter was 3800 A. The PGT analyzer showed that Fe/26 and Cr/24 were the primary elements contained in the pellet ejected from the 304 stainless steel target.

Approved for public release; distribution unlimited.

Laser Induced Evaporation from
Stainless Steel Surfaces

by

Zen Wen Hwang
Lieutenant, Republic of China Navy
B.S., Chung Cheng Institute of Science and Engineering, 1972

Submitted in partial fulfillment of the
requirements for the degree of

MASTER OF SCIENCE IN PHYSICS

from the

NAVAL POSTGRADUATE SCHOOL
December 1978

ABSTRACT

Laser-induced evaporation from a stainless steel surface was the laser-target damage mechanism which was studied. Infrared laser pulses with irradiances higher than 10^9 W/cm² were produced by a Q-switched neodymium glass laser. Experiments were performed in a vacuum chamber evacuated to about 10^{-6} Torr. The mass of evaporated material, area of laser-drilled hole and depth of damaged hole were measured. Results showed that the mass of evaporated material was proportional to $F^{1/2}$ where F is the laser flux in W/cm². Surface damage phenomena were studied by metallographic methods using an optical microscope and scanning electron microscope (SEM). Evaporated materials were partially collected and analyzed separately with the SEM and Princeton Gamma Tech (PGT) 1000 x-ray analyzer. Results for 40 laser shots on one target showed the deposition of small pellets on the collector. The number of pellets depends on the number of laser shots. After 40 shots a pellet density of 10^8 particles/cm² with an average particle separation of 10^{-4} cm was observed. The average particle diameter was 3800 \AA . The PGT analyzer showed that Fe/26 and Cr/24 were the primary elements contained in the pellet ejected from the 304 stainless steel target.

TABLE OF CONTENTS

I.	INTRODUCTION -----	8
II.	BACKGROUND AND THEORY -----	11
	A. HEATING WITHOUT PHASE CHANGE -----	11
	1. Assumption -----	11
	2. Temperature Increase Due to Absorption of Heat -----	11
	B. LASER-INDUCED MELTING -----	15
	1. General Statement -----	15
	2. Calculation of Depth Melted -----	18
	C. LASER-INDUCED EVAPORATION -----	24
	1. Classification -----	24
	2. Non Q-Switched Laser-Induced Evaporation	25
	3. Models -----	27
	a. Model 1 -----	27
	b. Model 2 -----	29
III.	Q-SWITCHED LASER-INDUCED EVAPORATION -----	32
	A. PHENOMENA -----	32
	B. MODELS -----	32
	1. The Superheated Metal -----	33
	2. The Heat-absorbing Plasma -----	35
	a. ANISIMOV's model -----	35
	b. CARUSO's model -----	38
	C. RECOIL PRESSURE AND MOMENTUM TRANSFER -----	42

IV.	EXPERIMENT -----	46
A.	APPARATUS -----	46
1.	Laser System -----	46
2.	Test Chamber -----	46
3.	Targets and Collectors -----	47
4.	Scanning Electron Microscope -----	48
5.	PGT Microanalysis System -----	49
6.	Optical Microscope -----	49
B.	PROCEDURES -----	50
1.	Surface Damage Studies -----	50
2.	Studies of Deposits on Collector -----	51
V.	RESULTS AND DISCUSSIONS -----	59
A.	COMPARISON OF SURFACE DAMAGED BY ONE SHOT WITH CERTAIN LASER ENERGY TO THE DAMAGED SURFACE BY THE SAME AMOUNT OF ENERGY INTEGRATED OVER SEVERAL SMALL ENERGY SHOTS -----	59
B.	MASS OF EVAPORATION -----	60
C.	DEPTH OF DAMAGED HOLE -----	62
D.	AREA OF DAMAGED HOLE -----	62
E.	METALLOGRAPH OF DAMAGED SURFACE -----	63
F.	ANALYSIS OF COLLECTOR SURFACE -----	65
VI.	CONCLUSIONS AND RECOMMENDATIONS -----	86
	APPENDIX A: THE LASER SYSTEM -----	89
	APPENDIX B: THE SCANNING ELECTRON MICROSCOPE -----	92
	LIST OF REFERENCES -----	97
	INITIAL DISTRIBUTION LIST -----	100

ACKNOWLEDGMENT

I wish to thank technician Robert Sanders for his assistance in the calibration, repair and maintenance of all equipment necessary to undertake this thesis. Also, his assistance in the design of the target-collector sets was invaluable. I would also like to express my sincere thanks to Professor F.R. Schwirzke for his help and guidance throughout this thesis and for his constructive comments during its writing. Finally, I want to thank my classmate, Lt. John H. Cocowitch, for his help in English grammar and smoothness of the sentences written in this thesis.

I. INTRODUCTION

The phenomenon of laser-target interaction has been studied in many previous experiments. The results are very important in understanding the damage mechanisms when laser radiation is absorbed by metal surfaces. These damage mechanisms are generally considered to be (1) heating of the metallic surface with no phase change, (2) change of phase of the surface, and (3) laser-induced particle emission from the surface.

When the energy flux is insufficient to melt or to vaporize the metal, heat conductivity is the principle factor responsible for energy transfer from the irradiated surface area into the bulk material. Previously, such a mechanism has been studied and reported by Polk [1].

When the energy flux is increased, melting or vaporization of the material occurs. The vaporized material produced in a laser-drilled hole has an associated pressure which flushes a layer of molten material off the walls of the hole and ejects it to the outside. A portion of the absorbed laser energy imparts kinetic energy to this evaporated and molten material. As the laser pulse becomes shorter and more powerful, the evaporated and molten material increases its kinetic energy although the amount of this material decreases. Furthermore, with an increase in laser irradiance the temperature on the evaporation front

and the internal energy of the vapor increase such that the total energy required for evaporation of a unit mass of the material increases [2].

As the laser irradiance level continues to increase, charged particle emission begins to occur at the irradiated surface. This particle emission mechanism has been extensively studied in terms of electron emission [3], thermionic emission of ions [4,5,6,7], neutral molecule emission [8], plasma production [9,10] and generation of shock waves [11]. Additionally, when light interacts with matter there exists a resultant recoil pressure and recoil momentum [12]. This recoil phenomenon is primarily associated with the second and the third damage mechanisms discussed above.

The primary problem which was undertaken in this thesis was to understand the damage mechanisms of laser-target interaction and to document the resultant metallographic damage. This also included an examination of the area and the depth of the laser-drilled hole. Of secondary importance was the examination of the relationship between the mass of evaporated material and the laser irradiance.

A Q-switched Neodymium-glass laser emitting 1-10 joule with a pulse width of 25 nsec (FWHM) was used to irradiate the surface of stainless steel targets. The targets were located in a vacuum chamber evacuated to about 10^{-6} Torr. When the laser beam was focused down to a focal area of 10^{-2} cm², typical irradiances of 10^{10} w/cm² were achieved

on the target surfaces. The area and the depth of the laser-drilled crater were then determined by employing metallographic techniques. The mass of the target material evaporated was determined by weighing the target before and after each experiment. Additionally, a portion of the evaporated target material was collected and analyzed using a scanning electron microscope (SEM) and a Princeton Gamma Tech (PGT) x-ray microanalysis system.

The results showed that the depth and the area of the laser-drilled crater, as well as the evaporated mass, were proportional to the laser irradiance. The x-ray spectrum analyzer revealed that some of the components of the evaporated 304 stainless steel were Fe/26 and Cr/24. The scanning electron microscope revealed that small pellets of about 0.03 to 0.3 μ size were emitted from the laser heated target spot. These pellets were captured on the collector plate placed 2 cm from the target. After 40 shots a pellet density of about $10^8/\text{cm}^2$ was found on the collector plate. This corresponds to a separation distance of about 10^{-4} cm between particles which had been captured on the collector.

II. BACKGROUND AND THEORY

In order to achieve a general comprehension of laser-induced damage mechanisms, one needs to understand the heating effect due to the absorption of light energy. Therefore, the three principle damage mechanisms are presented in detail in the following sections.

A. HEATING WITHOUT PHASE CHANGE

1. Assumption

To simplify the problem, it is helpful to make the following assumptions:

- (a) The heat flow is one-dimensional, i.e., the dimensions of the laser beam are large compared to the depth of penetration of the heat. The laser beam power density is assumed to be constant over the focal spot.
- (b) Reradiation of energy from the surface is negligible.
- (c) The thermal properties of the absorbing material are independent of temperature.
- (d) No change from solid to liquid phase occurs to provide simplicity of treatment [13].

2. Temperature Increase Due to the Absorption of Heat

The classical thermodynamic heat flow equation is given by

$$\bar{\nabla} \cdot \bar{J}(\bar{r}, t) + \rho c \frac{\partial T(\bar{r}, t)}{\partial t} = Q(\bar{r}, t) \quad (2-1)$$

where

$$\bar{J} = \text{heat flux } \left[\frac{\text{J}}{\text{cm}^2 \text{-sec}} \right].$$

$$\rho = \text{density of metal target } \left[\frac{\text{g}}{\text{cm}^3} \right].$$

$$c = \text{specific heat of metal target } \left[\frac{\text{J}}{\text{g-}^\circ\text{K}} \right].$$

$$T = \text{temperature } [^\circ\text{K}].$$

$$Q = \text{net energy per unit volume per unit time generated by absorbed photons } \left[\frac{\text{J}}{\text{cm}^3 \text{-sec}} \right].$$

The relation between heat flux and temperature is given by Fourier's law:

$$\bar{J}(\bar{r}, t) = - \bar{K} \bar{\nabla} T(\bar{r}, t) \quad (2-2)$$

where

$$\bar{K} = \text{thermal conductivity tensor.}$$

Substituting equation (2-2) into equation (2-1) yields

$$\nabla^2 T(\bar{r}, t) - \left(\frac{\rho c}{\bar{K}} \right) \frac{\partial T(\bar{r}, t)}{\partial t} = - \frac{Q(\bar{r}, t)}{\bar{K}}. \quad (2-3)$$

For the one-dimensional case \bar{K} , the three-dimensional conductivity tensor, is defined equal to σ , the thermal conductivity coefficient of the material. Also, κ , the thermal diffusivity, is defined equal to $\bar{K}/\rho c$ which equals $\sigma/\rho c$ for the one-dimensional case. Then the differential equation for heat flow in a semi-infinite slab of material with a boundary at $x = 0$ is:

$$\frac{\partial^2 T(x,t)}{\partial x^2} - \frac{1}{\kappa} \frac{\partial T(x,t)}{\partial t} = - \frac{Q(x,t)}{\sigma} \quad (2-4)$$

Laser energy is absorbed at the surface of a metal. This absorbed energy is proportional to the laser irradiance and the characteristic absorption coefficient, α . The absorbed energy will be exponentially dissipated as it penetrates into the metal surface. Thus, the remaining energy arriving at a depth, x , and a time, t , is given by

$$Q(x,t) \approx F(t) \alpha e^{-\alpha x} . \quad (2-5)$$

In the above equation

$$F(t) \equiv (1 - R) I_0$$

where I_0 is the laser irradiance and R is the reflectivity of the metal.

Solutions to the heat flow equation (2-4) can be determined for the following cases [14].

Case 1:

The absorption coefficient, α , is relatively small for a certain metal. This means that α is of the order of less than 10^5 cm^{-1} . The temporal pulse is rectangular in shape. In other words, $F(t) = F_0 = \text{constant}$ for $t > 0$. The solution to the heat flow equation (2-4) for these parameters is then given by

$$\begin{aligned}
 T(x,t) = & \left(\frac{2F_0}{\sigma}\right) (\kappa t)^{\frac{1}{2}} \text{ierfc}\left[\frac{x}{2(\kappa t)^{1/2}}\right] - \left(\frac{F_0}{\alpha\sigma}\right) e^{-\alpha x} \\
 & + \left(\frac{F_0}{2\alpha\sigma}\right) e^{(\alpha^2 \kappa t - \alpha x)} \text{erfc}\left[\alpha(\kappa t)^{\frac{1}{2}} - \frac{x}{2(\kappa t)^{1/2}}\right] \\
 & + \left(\frac{F_0}{2\alpha\sigma}\right) e^{(\alpha^2 \kappa t + \alpha x)} \text{erfc}\left[\alpha(\kappa t)^{\frac{1}{2}} + \frac{x}{2(\kappa t)^{1/2}}\right] \quad (2-6)
 \end{aligned}$$

In the above equation, erfc and ierfc denote the complementary error function and its integral.

Case 2:

The absorption coefficient α is large. For a metal, α is assumed to be of the order of 10^5 to 10^6 cm^{-1} . The laser pulse is still rectangular. The solution to the heat flow equation (2-4) for this case is given by

$$T(x,t) = \left[\frac{2F_0 (\kappa t)^{1/2}}{\sigma}\right] \text{ierfc}\left[\frac{x}{2(\kappa t)^{1/2}}\right]. \quad (2-7)$$

For $x = 0$,

$$T(0,t) = \left(\frac{2F_0}{\sigma}\right) \left(\frac{\kappa t}{\pi}\right)^{1/2}. \quad (2-8)$$

This equation then becomes very useful in estimating the approximate rise of the metal's surface temperature.

Case 3:

The absorption coefficient, α , is large and is the same order of magnitude as described in case 2. The laser pulse varies in time. A typical pulse used for calculations is shown in Fig. 2-1. The solution to the heat flow equation (2-4) for this case leads to the following result:

$$T(x,t) = \int_x^\infty \int_0^t \frac{F(\tau)}{F_0} \frac{\partial}{\partial \tau} \frac{\partial T'(x',t-\tau)}{\partial x'} dx' d\tau. \quad (2-9)$$

Numerical integration using Simpson's rule was employed to solve the above equation. A number of cases have been studied using time varying laser pulses and different absorbing metals. A typical result for a copper sample initially at 0 °C is shown in Fig. 2-2.

B. LASER INDUCED MELTING

1. General Statement

As the laser irradiance level becomes higher, the temperature of the metal surface reaches the melting point. Then a phase change occurs between the solid and liquid phases of the irradiated metal. Therefore, the irradiances considered in this damage mechanism must be high enough to melt the metal surface but not high enough to vaporize it.

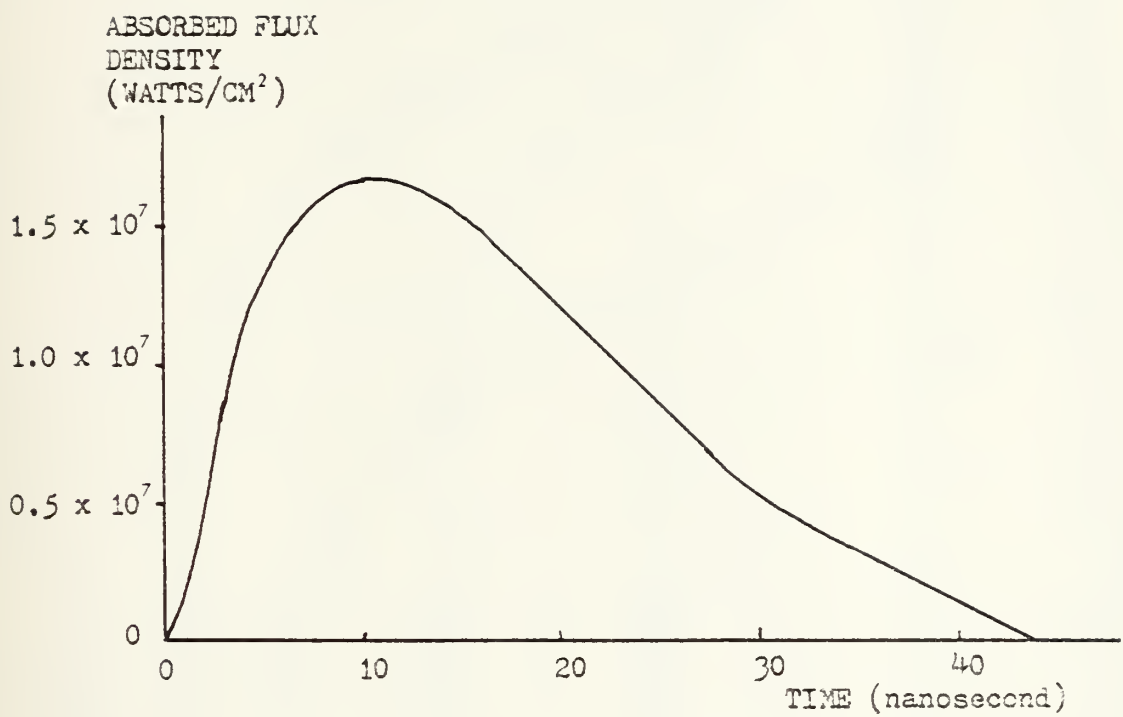


Fig. 2-1. Time varying laser pulse shape used for calculation in case 3.
[From J.F. Ready, J. Appl. Phys. 36, 462(1965)]

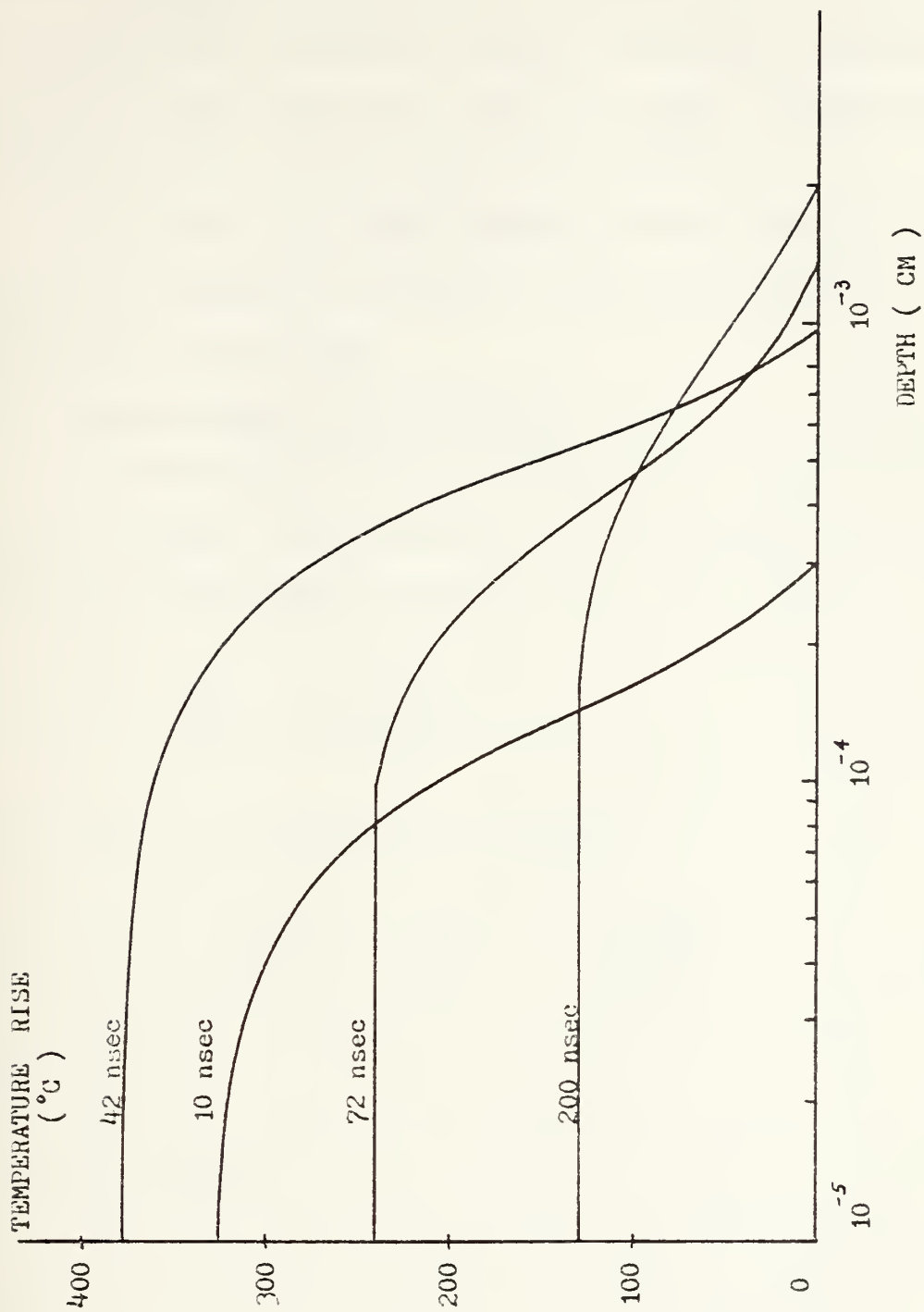


Fig. 2-2 Calculated temperature rise as a function of depth, with time as a parameter, caused by absorption of a Q - switched laser pulse in copper.

[From J. F. Ready, J. Appl. Phys. 36, 462 (1965)]

Q-switched lasers are usually not suitable for studies of laser-induced melting damage because the pulse widths are too short and the irradiance levels too high. These high irradiance levels vaporize the metal surface.

In solving the laser-induced melting problem the assumptions presented in Section A are again used to simplify the calculations.

2. Calculation of Depth Melted

A semi-infinite slab of material was used to model the metal surface. The following set of equations describe the melting of the metal originally at 0 °C: [14]

$$\frac{\partial T_i}{\partial t} = \kappa_i \frac{\partial^2 T_i}{\partial x^2} \quad (2-10)$$

where $i = 1, 2$ 1 = liquid, 2 = solid.

$$-\sigma_1 \frac{\partial T_1}{\partial x} + \sigma_2 \frac{\partial T_2}{\partial x} = \rho L \frac{dX(t)}{dt} \quad (2-11)$$

where

$$x = X(t),$$

and

$$T_1 = T_2 = T_m ; \quad x = X(t) , \quad t > 0$$

$$-\sigma_1 \frac{\partial T_1}{\partial x} = F ; \quad x = 0 , \quad t > 0 .$$

Also,

$$\lim_{x \rightarrow \infty} T_2(x, t) = 0$$

$$T_2(x, 0) = T_s(x) ; \quad X(0) = 0 ,$$

where

$x = X$ the location of the fusion interface [cm].

x = depth beneath surface [cm].

T_m = melting temperature of metal [$^{\circ}\text{K}$].

$T_s(x)$ = the temperature distribution in the solid when melting begins [$^{\circ}\text{K}$].

F = laser flux density [$\frac{\text{W}}{\text{cm}^2}$].

L = latent heat of fusion [$\frac{\text{erg}}{\text{cm}^2 \cdot \text{g}}$].

σ_1 = conductivity of liquid metal [$\frac{\text{W}}{\text{cm} \cdot ^{\circ}\text{K}}$].

σ_2 = conductivity of solid metal [$\frac{\text{W}}{\text{cm} \cdot ^{\circ}\text{K}}$]

κ_1 = diffusivity of liquid metal [$\frac{\text{cm}^2}{\text{sec} \cdot ^{\circ}\text{K}}$]

κ_2 = diffusivity of solid metal [$\frac{\text{cm}^2}{\text{sec} \cdot ^{\circ}\text{K}}$].

The time from the start of the laser pulse until surface melting begins is given by [15]:

$$t_m = \frac{\pi \sigma_2^2 T_m^2}{4 \kappa_2 F^2} \quad (2-12)$$

The function $T_s(x)$ gives the temperature distribution in the solid when melting begins and can be determined for the three different cases presented in Section II.A. To solve equation (2-11), Cohen used analog computer techniques. The results are given in terms of the variables T' and X' defined by [16]:

$$T' = \frac{T(0,t)}{T_m} \quad (2-13)$$

$$X' = \frac{100 L F X}{3\pi T_m^2 C_2 \sigma_2} \quad (2-14)$$

Figure 2-3 illustrates T' , the normalized surface temperature, versus t/t_m , the normalized time after melting begins. Figure 2-4 illustrates X' , the normalized depth melted, versus t/t_m . The conditions assumed are that the thermal conductivities and diffusivities of the molten and solid phases are equal. The ratio, Y , of latent heat to heat content which appears in the caption of Figures 2-3 and 2-4 is defined equal to $L/C_2 T_m$, where C_2 is the specific heat per unit mass of the metal and T_m is the melting point of the metal.

As a specific example, laser-induced depths of melting in yellow brass have been studied [15]. The results are shown in Figure 2-5 for several laser irradiances.

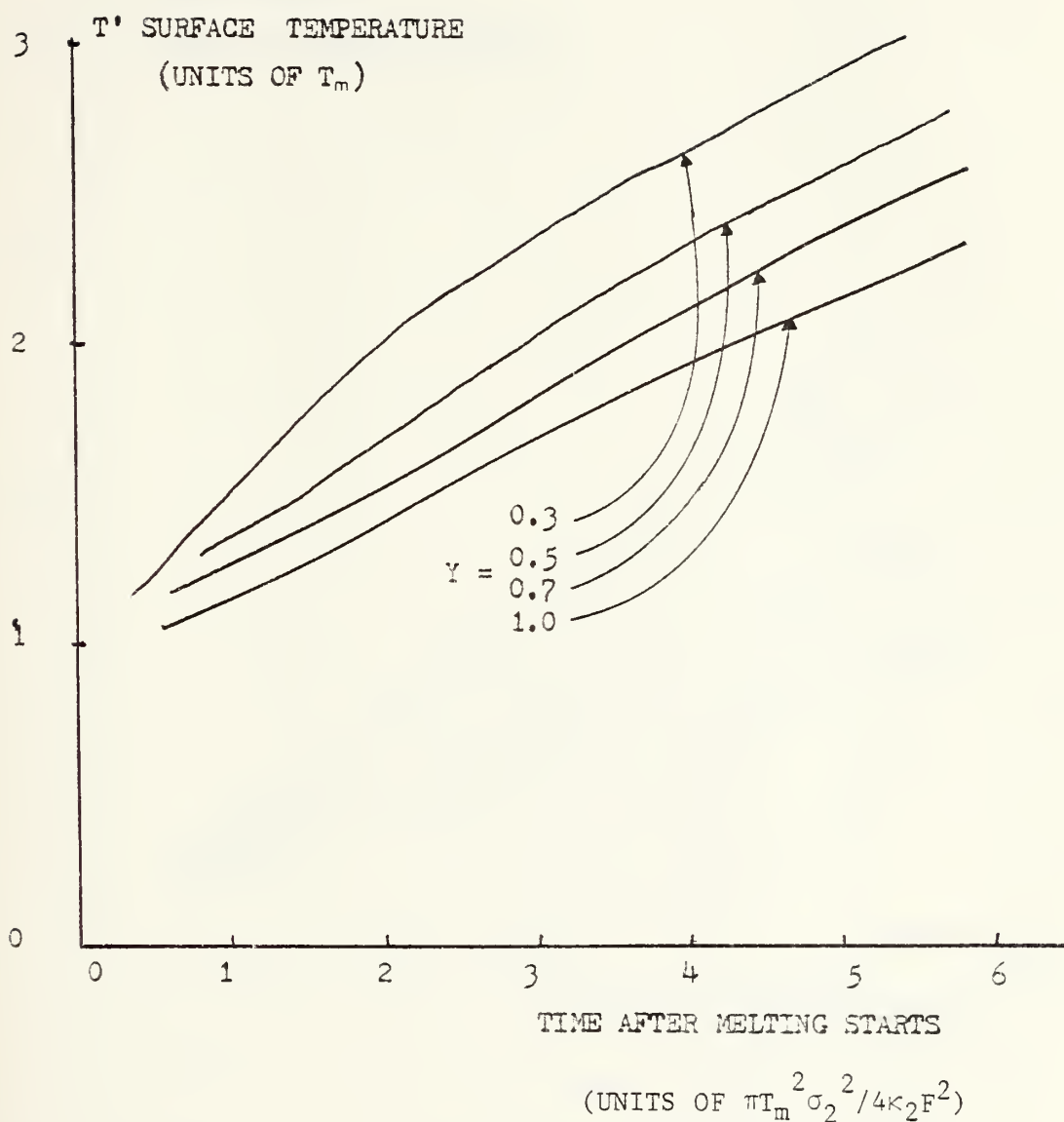


Fig. 2-3. The normalized surface temperature as function of normalized time after melting begins for various ratios Y of latent heat to heat content at the melting point, T_m .
 [From M.I. Cohen, J. Franklin Inst. 283, 271 (1967)]

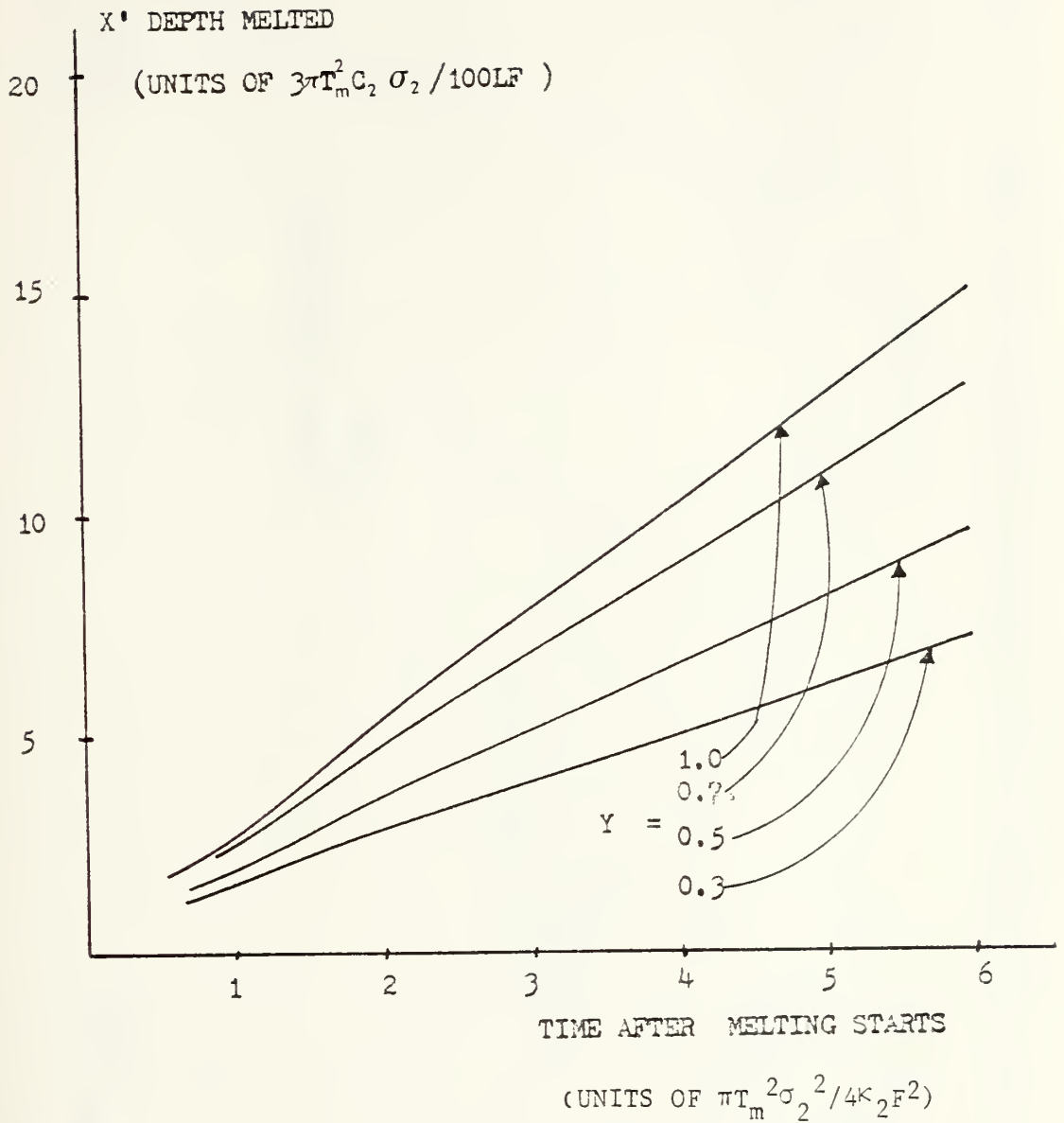


Fig. 2-4. The normalized depth melted as function of normalized time after melting begins for various ratios Y of latent heat to heat content at the melting point, T_m . [From M.I. Cohen, J. Franklin Inst. 283, 271 (1967)]

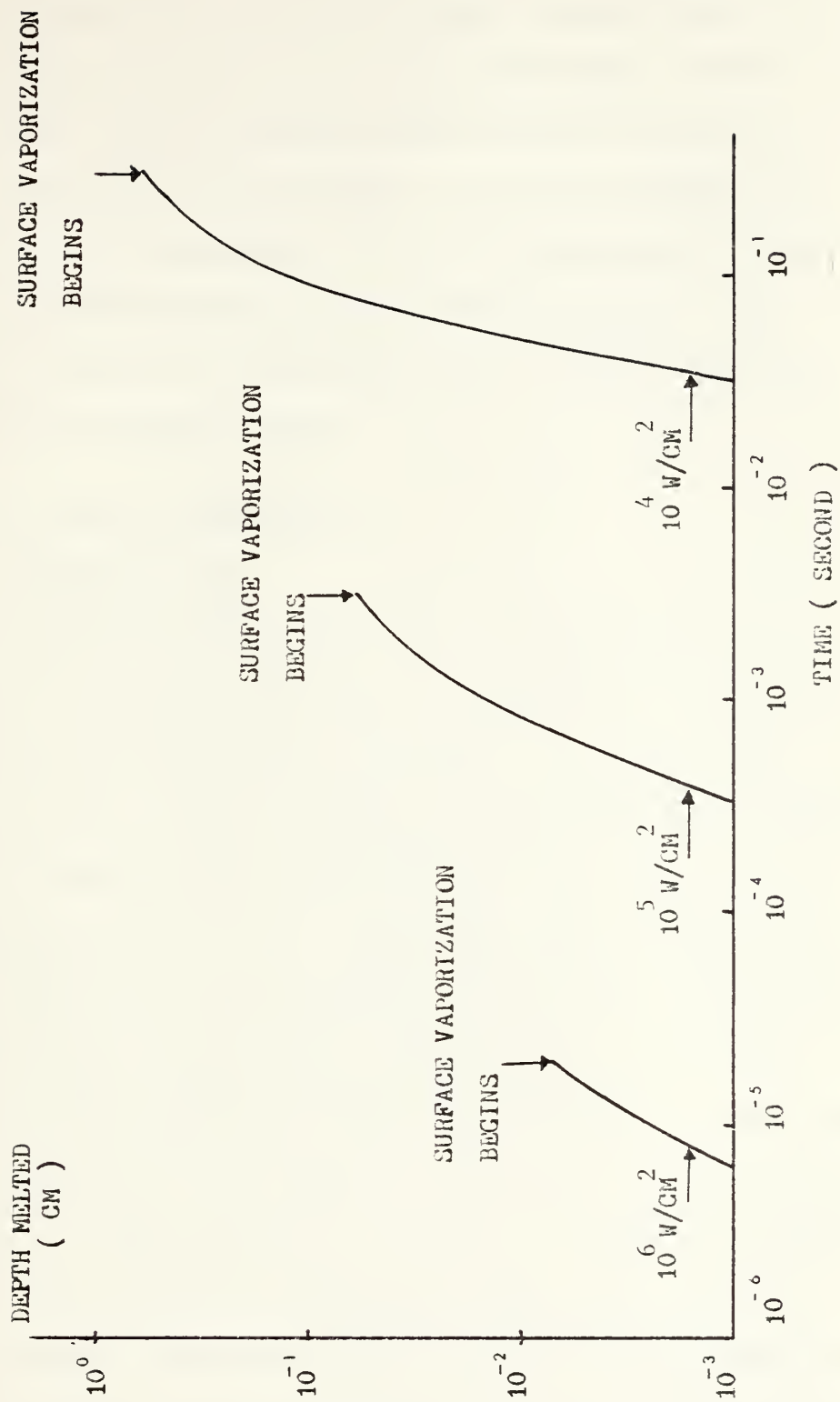


Fig. 2-5. Melted depth in yellow brass as a function of time for several laser irradiances.
 [From J.F. Ready, "Effects of High Power Laser Radiation," AP (1971)]

This figure indicates the relatively limited depth of melting particularly for high flux densities. These results show that the maximum depth melted for non Q-switched lasers is on the order of a few hundreds to a few tenths of a millimeter. For an unfocused Q-switched laser which normally has a flux density greater than 10^6 W/cm^2 , figure 2-5 indicates that melting would be negligible for yellow brass.

C. LASER-INDUCED EVAPORATION

1. Classification

In the case of laser-induced evaporation, it is sufficient to concentrate only on evaporation without considering the existence of melting. At high laser irradiances the surface temperature of a metal will rapidly rise to its vaporization temperature. For example, at an irradiance of 10^9 W/cm^2 , the vaporization temperature of most metals will be reached in less than 1 nanosecond [15]. After the vaporization temperature is reached, the input power begins to supply the necessary latent heat of evaporation to a thin layer of material at the surface. This leads to the concept of a layer of vaporizing material of some finite thickness separating the solid and the gaseous phases. Therefore, the use of a thermodynamic model is not applicable. This phenomenon usually occurs with a Q-switched laser pulse heating. For non Q-switched lasers the power densities are lower and the pulsewidths are

longer, therefore the material vaporized can be removed fast enough from the surface so that this layer is not established. Thus, common thermodynamic concepts are valid for non Q-switched laser-induced evaporation. For this reason, non Q-switched laser-induced evaporation and Q-switched laser-induced evaporation will be discussed separately.

2. Non-Q-Switched Laser Induced Evaporation

For a one dimensional semi-infinite slab of metal, the heat conduction is governed by thermodynamic mechanisms. The surface temperature rises to a vaporization point, T_v , and vaporization starts as the metal absorbs the laser energy. The surface, initially at $x = 0$, moves inward and at time, t , is at position $X(t)$. The heat flow equation describing this process in the metal is:

$$\frac{\partial^2 T(x,t)}{\partial x^2} = \left(\frac{1}{\kappa}\right) \left(\frac{\partial T(x,t)}{\partial t}\right), \quad x > X(t) \quad t > 0 \quad (2-15)$$

with initial and boundary conditions given by

$$T(x,0) = 0$$

$$T(x,t) \rightarrow 0 \quad \text{as} \quad x \rightarrow \infty, \quad t > 0$$

$$T(X(t),t) = T_v$$

where T_v is the vaporization temperature, and the other variables are defined as before.

Input heat flux is divided into two fractions. One is the heat flow by conducting into the metal, and the other is used to vaporize the material. That is:

$$F(t) = -\sigma \left(\frac{\partial T}{\partial x} \right) + \rho L \left(\frac{\partial X(t)}{\partial t} \right), \quad x = X(t), \quad t > 0 \quad (2-16)$$

where

L = latent heat of evaporation per unit mass.

At low irradiances the conduction term is more significant. As the laser flux density increases, it reaches a value at which the heat is supplied too fast to be conducted away. The dominant factor then becomes the latent heat of evaporation. The crossover of the input heat flux from the region in which the thermal conductivity is dominant to the region in which the effect of thermal conductivity is negligible is given approximately by

$$F_c \geq 2 L \rho \kappa^{\frac{1}{2}} \tau^{-\frac{1}{2}} \quad (2-17)$$

where

τ = laser pulse width,

and the other variables are defined as before.

Typical values of the cross over heat flux are in the range of 10^6 - 10^7 W/cm² for a non Q-switched laser.

Now several models are presented which calculate the amount of evaporated material from the irradiated surface.

3. Models

There are several models that can solve this problem. For simplicity, only two models are considered in the following section.

a. Model 1

This model assumes one-dimensional heat flow, a continually vaporizing surface with constant heat input at the surface, and continual removal of the vaporized material from the surface [17].

It is known that the time to reach the evaporation point depends upon the particular material and the laser irradiance. The equation to describe this situation is:

$$t_v = \left(\frac{\pi}{4}\right) \left(\frac{\sigma \rho C}{F^2}\right) (T_v - T_o)^2 \quad (2-18)$$

where

t_v = time at which evaporation is reached.

T_v = the vaporization temperature.

T_o = initial temperature.

When the material absorbs a large constant heat flux which is greater than the crossover flux it begins vaporizing after time, t_v . The rate of material removal approaches a steady state rate given by:

$$V_{ss} = \frac{F}{\rho[L + c(T_v - T_o)]} \quad (2-19)$$

The depth of vaporization would then be expressed by

$$D = V_{ss} \cdot t_v$$

Using Zn metal as an example,

$$t_v = 1.277 \text{ } \mu\text{sec} \quad \text{for} \quad F = 10^6 \text{ W/cm}^2$$

and

$$\sigma = 0.2 \frac{\text{cal}}{\text{cm}^3 \cdot ^\circ\text{C} \cdot \text{sec}}, \quad \rho = 7.14 \frac{\text{g}}{\text{cm}^3},$$

$$C = 0.0915 \frac{\text{cal}}{\text{g} \cdot ^\circ\text{C}}, \quad L = 27.4 \frac{\text{K-cal}}{\text{g}},$$

$$T_v = 906 \text{ } ^\circ\text{C}, \quad T_o = 26 \text{ } ^\circ\text{C}$$

and

$$\begin{aligned}
 V_{ss} &= \frac{10^6 \cdot \frac{1}{4.2} [\text{cal/sec-cm}^2]}{7.14 \left[\frac{\text{g}}{\text{cm}^3} \right] [27400 \left[\frac{\text{cal}}{\text{g}} \right] + 0.0915 \left[\frac{\text{cal}}{\text{g-}^\circ\text{C}} \right] (906-26) [^\circ\text{C}]} \\
 &= \frac{10^6}{8.2 \times 10^5} \left[\frac{\text{cal}}{\text{sec-cm}^2} \right] \cdot \frac{1}{\left[\frac{\text{g}}{\text{cm}^3} \right] \left[\frac{\text{cal}}{\text{g}} \right]} \\
 &= 1.22 \frac{\text{cm}}{\text{sec}} .
 \end{aligned}$$

Then

$$\begin{aligned}
 D &= V_{ss} \cdot t_v = 1.22 \left[\frac{\text{cm}}{\text{sec}} \right] \cdot [1.277 \times 10^{-6}] [\text{sec}] \\
 &= 1.56 \text{ } \mu\text{cm}.
 \end{aligned}$$

b. Model 2

This model uses a temperature higher than the normal vaporization temperature at the moving boundary between vapor and solid interface [18].

The steady state vaporization velocity is then given by (from equation (2-19)):

$$V_{ss} = \frac{F}{\rho [cT' + L]} \quad (2-20)$$

where T' = temperature of the surface which is greater than the normal boiling point of material, i.e., $T' > T_v - T_o$.

From Boltzmann's distribution

$$\frac{dn}{dt} = n v_o e^{-Lm/N_o kT} \quad (2-21)$$

where

n = the surface density of atoms $[\frac{\text{atom}}{\text{cm}^3}]$

v_o = the Debye frequency ($\approx 10^{13} \text{ sec}^{-1}$)

m = the atomic weight [g]

N_o = Avogadro's number = $6.02 \times 10^{23} [\text{mole}^{-1}]$

k = Boltzmann's constant = $1.38 \times 10^{-23} [\frac{\text{J}}{\text{°K}}]$

L = latent heat of evaporation per unit mass $[\frac{\text{cal}}{\text{g}}]$.

This equation essentially gives the rate of escape of atoms from the surface.

The velocity, V_{ss} , can be expressed in terms of dn/dt , namely

$$V_{ss} = (\frac{dn}{dt}) \cdot h_a \cdot \frac{1}{n} \quad (2-22)$$

where

h_a = thickness of one atomic layer [cm].

Then combining equation (2-21) with (2-22) yields

$$V_{ss} = h_a v_o e^{-Lm/N_o kT} \quad (2-23)$$

Also, combining equation (2-20) and (2-21) gives the relation between F and T'. This result is

$$F = h_a v_o \rho [cT' + L] e^{-Lm/N_o kT'} \quad (2-24)$$

Again, Zn is used as an example. First, from equation (2-24) using iterative techniques to solve for T', $T' = 17,450$ °K. The atomic layer, h_a , was calculated to be 2.76×10^{-8} cm. Then $V_{ss} = 1.18$ cm/sec and depth, $D = 1.51$ μ cm. These results are not much different from the results of model 1.

III. Q-SWITCHED LASER-INDUCED EVAPORATION

A. PHENOMENA

As the power densities of Q-switched lasers increase higher than 10^9 W/cm² on a target surface, the evaporation behavior becomes different from the evaporation behavior of non Q-switched lasers. Three important associated phenomena are presented in the following paragraphs.

The influence of the blowoff material emitted from the surface on the incoming laser radiation must be considered. The presence of this material modifies the interaction of the laser radiation with the surface. First, it exerts a pressure on the surface [19]. This changes the evaporation characteristics of the surface. Second, the blowoff material absorbs light and shields the surface from the laser radiation. Finally, as the blowoff material becomes very hot, it can produce an impulse reaction on the surface and a shock wave propagates into the metal.

Therefore a Q-switched laser pulse produces not only laser-target interaction, but also vapor-target interaction.

B. MODELS

For the Q-switched laser-induced vaporization mechanism the following representative models are used to describe and calculate the amount of evaporation from the metal surface.

1. Superheated Metal

The surface of the metal rises to the vaporization temperature and begins to vaporize. This material recoils against the surface and produces a high pressure. This pressure pulse raises the boiling point of the underlying material which becomes superheated as more heat is conducted into the interior of the material [13].

This model has given reasonable agreement with previously determined results [18] for a laser flux density of 10^9 W/cm^2 , but it has not been tested over a wide range of laser flux densities.

The equations used to calculate the superheated temperature and depths of evaporation on metal are equation (2-23) and equation (2-24). For clarity, equation (2-23) and (2-24) are rewritten,

$$V_{ss} = h_a \cdot v_o \cdot e^{-Lm/N_o kT'}$$

and

$$F = h_a \cdot v_o \cdot \rho [cT' + L] e^{-Lm/N_o kT'}$$

Table 1 shows a comparison between this model and an experiment conducted by Ready [13]. One can see that agreement is good.

This model was not applicable for the case of shielding of the surface from the incoming laser beam

TABLE 1
 DEPTH OF HOLE PRODUCED BY $44 - \text{N}$ SEC DURATION ,
 $10^9 \text{ W} - \text{CM}^{-2}$ LASER PULSE

MATERIALS	DEPTH CALCULATED ON BASIS OF SUPERHEATED METAL MODEL (μ)	MEASURED DEPTH (μ)
Stainless Steel	1.8	1.1
Brass	2.0	2.5
Al	6.2	3.6
Cu	3.0	2.2
Ni	2.4	1.2

[From J. F. Ready , J. of Appl. Phys. V36, 462, (1965)]

when the blowoff material became hot, ionized and opaque.

2. The Heat Absorbing Plasma

Early in the Q-switched laser pulse, a small amount of material is removed from the surface. This material can be heated further by absorption of the incoming laser radiation. It becomes thermally ionized and opaque to the incident radiation. The heat absorbing plasma prevents light from reaching the surface. Therefore, most of the energy in the laser pulse is absorbed by the material in front of the surface, and a relatively small fraction of laser radiation actually reaches the surface. Near the end of the laser pulse, the blowoff material becomes so hot that it begins to reradiate thermally. Some of this radiation may reach the surface and cause further vaporization [15].

Schematic representation of the depth vaporized on a metal target as a function of time by a high flux density pulse is shown in Figure 3-1.

Based on these phenomena, there are two models that specify the velocity of the evaporation front and surface temperature.

a. ANISIMOV's Model

ANISIMOV first assumed that the density of the laser energy flux was not excessively large so that there was no significant absorption of light by the blowoff vapor.

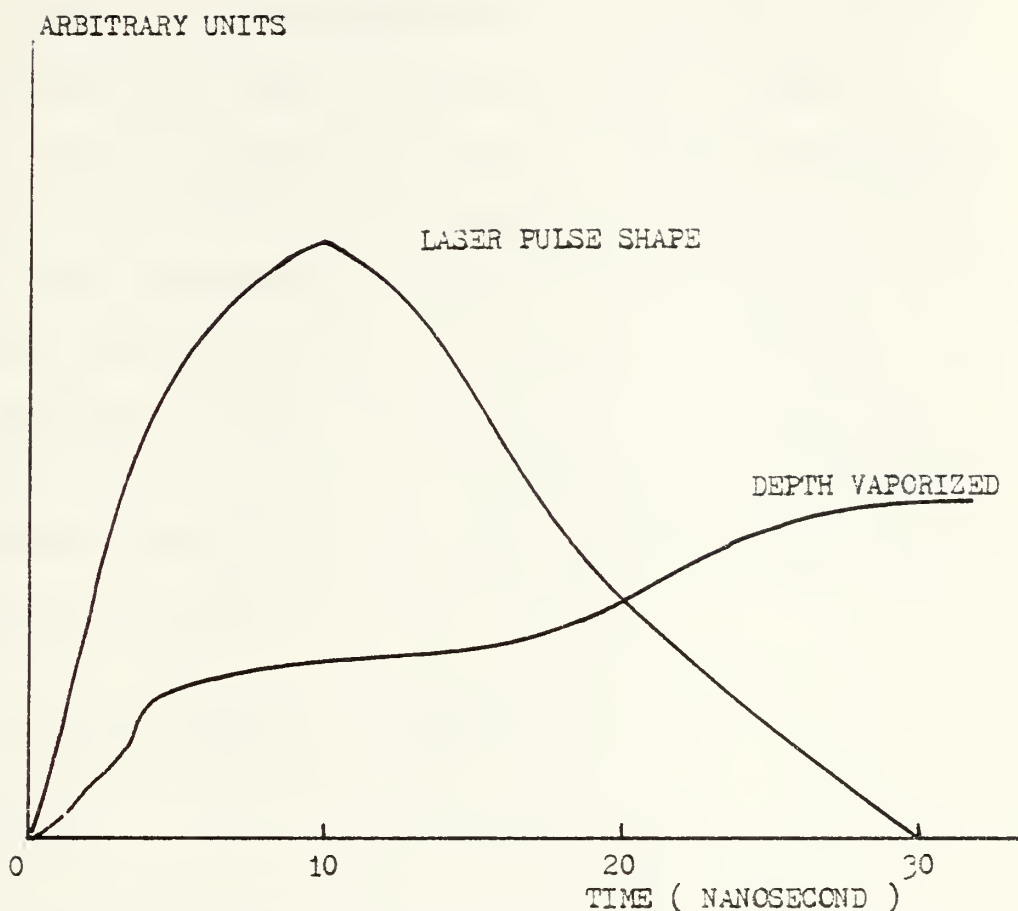


Fig. 3-1 Schematic representation of the depth vaporized in a metal target as function of time by a high flux density pulse with the indicated pulse length. Figure shows the effect of shielding of the target surface by blowoff material produced early in the pulse.

[From J. F. Ready "Effects of High Power Laser Radiation" AP (1971)]

It appeared that the ranges of flux densities over which the vapor absorption of laser light was insignificant was limited to the values, $10^9 - 10^{10}$ W/cm², for neodymium glass lasers and the majority of metals. The expansion of the vapor occurred in a centered rarefaction wave under the assumptions of a one-dimensional expansion and an ideal gas equivalent vapor. In the vicinity of the vaporizing surface, there is a region of several mean free path lengths which should be considered as a discontinuity surface in the hydrodynamic treatment of the problem. The boundary conditions relate the values of the hydrodynamic variables in the rarefaction wave to the surface temperature of the metal [20]. The following equations for the surface temperature and velocity of the vaporizing surface were obtained:

$$n_n(t) \left(\frac{kT}{m} \right)^{\frac{1}{2}} \left(L + \frac{2.2kT}{m} \right) = 3.1 F \quad (3-1)$$

and

$$v = \frac{F}{\rho \left[L + \frac{2.2kT}{m} \right]} \quad (3-2)$$

where

m = atomic mass [g]

ρ = metal density [$\frac{g}{cm^3}$]

$n(T)$ = the saturated vapor density as a function of temperature [$\frac{1}{cm^3}$].

The other variables are defined as before. Solutions of these two equations give the values of temperature and vaporization velocity. Finally, the depth is calculated by multiplying the vaporization velocity by the approximate duration of laser pulse.

For example, zinc can be evaporated by absorbing a $4 \times 10^9 \text{ W/cm}^2$ laser flux density. For this irradiance, the temperature may become as high as 18,000 °K. The associated vaporization velocity, v , would be $4.86 \times 10^6 \text{ cm/sec}$. Then the depth, $D = v \cdot \tau$, would equal $4.86 \times 10^6 \times 25 \times 10^{-9} \approx 1 \text{ mm}$.

b. CARUSO's Model

CARUSO, BERTOTTI and GUIPPONI have constructed a very useful model that is (1) able to describe the phenomena of three separate regions during laser-target interaction; (2) allows a calculation of the density of the resultant shock wave region; and (3) allows a calculation of the mass of material evaporated. This model can be used to describe the behavior of the hot plasma and the high density target material.

So far, the models have been limited to laser irradiance less than 10^{10} W/cm^2 . However, using CARUSO's model, the laser irradiance may go as high as 10^{12} W/cm^2 or even higher [21].

At the beginning the laser pulse interacts with the surface. Pretty soon the large and growing laser flux

input becomes sufficient to allow an electron avalanche break-down. Because the collision time of an electron in the dense material is about 10^{-13} sec and the pulse width is about 10^{-9} sec, the collision frequency is very high. Even a small degree of ionization is sufficient to make the plasma opaque to the laser beam. Thus, a large fraction of the optical energy is transformed into thermal energy. This occurs in a thin layer, F, shown in Figure 3-2. Complete ionization occurs in this thin layer within a short time.

The second phase of the laser target interaction is characterized by the emission of a hot and fast plasma jet, J, propagating in the direction of the light source. Due to the reaction force, a shock wave, s, is generated, which penetrates into the unperturbed region of the target. As the plasma further expands toward the light source, it again becomes transparent to the incident laser light.

The plasma parameters adjust themselves so that approximately 8% of the incident optical energy go into heating of the expanding plasma. This means the expanding plasma is almost transparent to the light.

Using this model and the parameters defined in Figure 3-2, the ratio of densities between the solid and the plasma jet is given by:

$$\frac{\rho_1}{\rho_2} = 5 a^{\frac{3}{8}} F^{-\frac{1}{4}} t^{\frac{3}{8}} \rho_1 \quad (3-3)$$

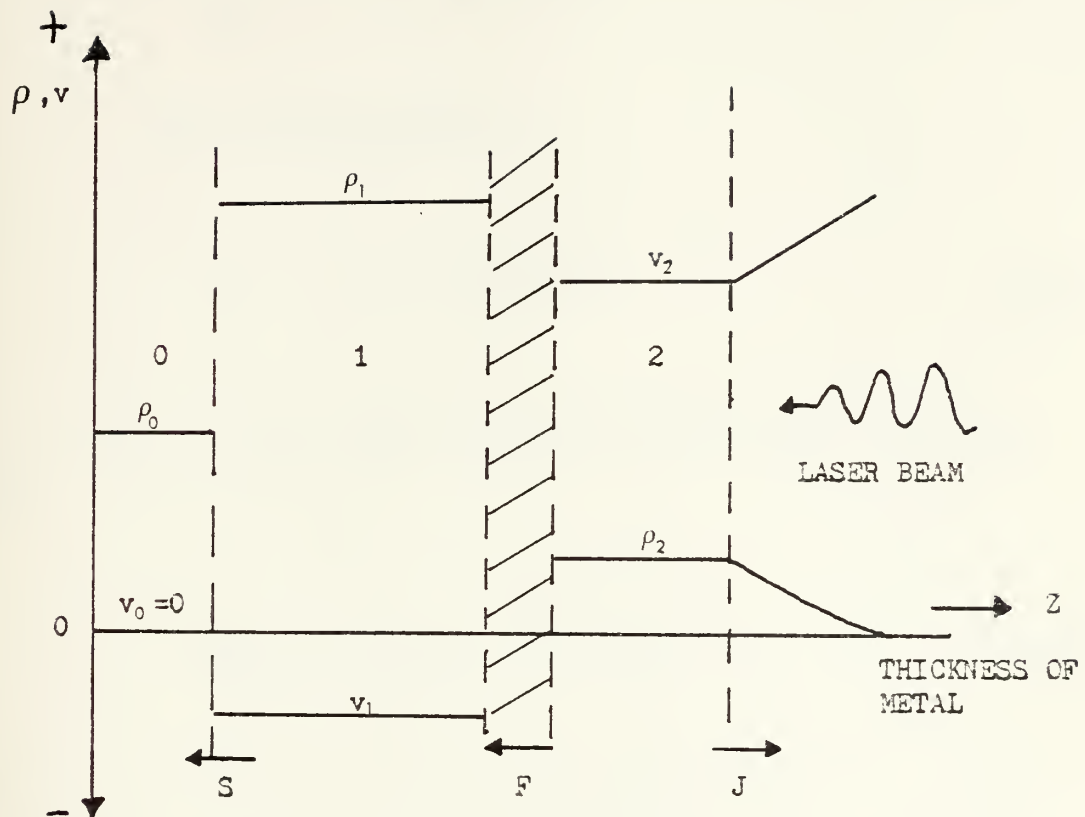


Fig. 3-2 Region 0 represents undisturbed material. Region 1 represents solid material which is shock compressed. Region F represents the location of the main energy absorption. Region 2 is a plasma jet. It shows that the density in region 1 is much greater than the density in region 2, and the density goes to zero after the plasma expansion.

[From A. Caruso, B. Bertotti and P. Giupponi, IL NUOVO CIMENTO 45B 176 (1966)]

The thermal velocity of the jet is

$$V_{th} = 0.8 a^{\frac{1}{8}} F^{\frac{1}{4}} t^{\frac{1}{8}} \quad (3-4)$$

The jet velocity is

$$V_2 = 1.47 a^{\frac{1}{8}} F^{\frac{1}{4}} t^{\frac{1}{8}} \quad (3-5)$$

and the mass of the plasma ejected at the time t , by one cm^2 is

$$m(t) = 0.39 a^{-\frac{1}{4}} F^{\frac{1}{2}} t^{\frac{3}{4}} \quad (3-6)$$

where

$$\rho = \text{metal density } \left[\frac{\text{g}}{\text{cm}^3} \right]$$

$$F = \text{laser irradiance } \left[\frac{\text{erg}}{\text{cm}^2 \cdot \text{sec}} \right]$$

$$t = \text{laser pulse width } [\text{sec}]$$

$$a = Z^3 \left(\frac{1+Z}{2} \right)^{\frac{3}{2}} \left(\frac{\omega_r}{\omega} \right)^2 A^{-\frac{7}{2}} \cdot 4 \cdot 10^{29} \left[\frac{\text{cm}^8}{\text{g}^2 \cdot \text{sec}^3} \right]$$

where

$$Z = \text{atomic number}$$

$$A = \text{mass number}$$

ω = angular frequency of light

ω_r = resonant frequency.

For a ruby laser,

$$\omega = \omega_r = 2.73 \times 10^{15} \text{ sec}^{-1}$$

with a flux density of $F = 10^{19} \text{ erg/cm}^2\text{-sec}$, and laser pulsewidth, $t = 10^{-9} \text{ sec}$, irradiating a solid hydrogen target, CARUSO found

$$\frac{\rho_1}{\rho_2} \approx 10^3, \quad v_2 \approx 3 \times 10^7 \frac{\text{cm}}{\text{sec}}.$$

This is a reasonably expected solution, since the critical plasma density for the ruby laser frequency is $n_c = 2.3 \times 10^{21} \text{ cm}^{-3}$ which is quite smaller than the solid hydrogen density of $4.25 \times 10^{22} \text{ cm}^{-3}$.

C. RECOIL PRESSURE AND MOMENTUM TRANSFER

As mentioned before, a shock wave is produced on the metal's surface when it absorbs a giant laser pulse. The momentum resulting from the blowoff of target material is given by the integral

$$M = A \int_0^t p(t) dt.$$

Taking the average of the recoil pressure, the relationship between momentum and the average recoil pressure is given by

$$\bar{P} = \frac{M}{A \cdot \tau} \quad (3-7)$$

where

\bar{P} = the average recoil pressure in the target [$\frac{\text{dyne}}{\text{cm}^2}$]

M = momentum transferred to the target material [dyne-sec]

A = area over which the pressure is applied [cm^2]

τ = the pulse width of laser [sec].

The average recoil pressures are on the order of 10^5 bars to 10^6 bars depending upon the material and laser irradiance. The average light intensity of a laser pulse is calculated as follows:

$$F = \frac{J}{A \cdot \tau} \left[\frac{\text{Watt}}{\text{cm}^2} \right] \quad (3-8)$$

where

J = energy in a particular giant pulse [joule]

A = area of the focal spot [cm^2].

GREGG and THOMAS' results [12] showed that there is an optimum intensity for each material which gives a maximum amount of momentum transfer per joule of laser energy. This maximum momentum transfer corresponds to a maximum of material evaporated. The optimum laser intensity is slightly different for different materials. The approximate reference value is about $5 \times 10^8 \text{ W/cm}^2$ of laser irradiance.

In addition to the momentum transferred due to the evaporated material, there is also a momentum transferred due to the incident laser light itself. The momentum due to the laser light was determined by GREGG and THOMAS to be $7 \times 10^{-4} \text{ dyne-sec/J}$. In comparison with the total momentum transferred (2 to 10 dyne-sec/J), one may neglect that portion of the momentum due to the laser light itself because it is very much less than the total. This was numerically proved by ASKAR'YAN and MOROZ [19]. The equation used to calculate the recoil pressure is:

$$P \approx \frac{\alpha F V_f}{\lambda} \quad (3-9)$$

where

V_f = the final velocity of vapor flow [$\frac{\text{cm}}{\text{sec}}$]

α = the portion of energy used in evaporation [constant].

$\lambda = L + \frac{1}{2} V_f^2$ is the total energy due to the latent heat of evaporation and the velocity of the vapor [$\frac{\text{cal}}{\text{g}}$].

The recoil pressure due to laser beam itself is:

$$P_1 = \frac{\alpha F}{C} \quad (3-10)$$

where

$C = \text{speed of light } [\frac{\text{cm}}{\text{sec}}]$.

Thus, the ratio of the recoil pressure, P , to the pressure, P_1 , of the beam is

$$\frac{P}{P_1} \approx \frac{C V_f}{\lambda} \quad (3-11)$$

Taking the worst case as an example, $V_f \geq 10^5$ cm/sec, $\lambda \approx 10^3$ cal/g, then, $P/P_1 \geq 10^4 \sim 10^5$. Therefore, it is justifiable to neglect the radiative pressure of the incident laser beam.

IV. EXPERIMENT

A. APPARATUS

The equipment used in this experiment consisted of a Neodymium glass laser system, a testing chamber and an optical microscope. For surface damage studies, a scanning electron microscope and PGT 1000 x-ray analyzer were utilized. Figure 4-1 shows a schematic of the experimental arrangement.

1. Laser System

The light source used in the laboratory was a Q-switched neodymium-doped glass laser which emits a wavelength of 1.06 micrometers. It has a 25 nanosecond (FWHM) pulse width. The unfocused beam has a cross sectional area of $4.04 \pm 0.2 \text{ cm}^2$ [1].

Stainless steel targets were located in a vacuum chamber which had a base pressure of about 10^{-6} Torr. The neodymium laser pulse struck the targets in the vacuum chamber at an angle of 30° (see Figure 4-5). A detailed description of this laser system is given in Appendix A.

2. Test Chamber

The main test chamber is made of unbaked aluminum. It has a volume of 12.9 ± 0.3 liters. A probe is used to hold the targets in the chamber. Several ports in the chamber provide for the mounting of various valves and gauges as well as an observation window. The vacuum

chamber has the capability of being evacuated to pressures of the order of 10^{-7} Torr by using a mechanical pump and an oil diffusion pump. The oil diffusion pump is cooled by liquid nitrogen which is introduced by way of a cold trap. The valves and piping system allow isolation of the chamber from the pumps. A gas bleed-off system allows for rapid flooding of the chamber for testing or for opening the chamber cover port. A detailed function of the gauges is given by [26]. The physical size and a detailed explanation of the chamber are given by Polk [1].

3. Targets and Collectors

The metal targets used were disks 0.5 ± 0.05 inches in diameter. Two kinds of targets were prepared. One was 0.125 ± 0.001 inches in thickness, and the other was 0.03125 ± 0.00005 inches in thickness. The disks were machined from 304 stainless steel stock. The thick targets were used in surface damage studies. The thin targets were used in the determination of mass evaporated, area of the damaged hole and depth of the hole. The thick targets were highly polished by a polishing machine and the thin targets were polished by using only a 0.05 micrometer Al_2O_3 slurry.

There were also two kinds of collectors used. One was polished, thick stainless steel which was exactly the same size as the thick target. The other was an aluminum stub 0.5 ± 0.05 inches in diameter which has a

leg that connects to the circuitry inside of the scanning electron microscope vacuum chamber.

The targets were held by an aluminum disk with a diameter of 2.0 ± 0.1 inches and a thickness of 0.25 ± 0.01 inch. A hole was drilled through the center of the target holder which allowed for mounting of the target holders on a rotating feedthrough into the test chamber. Collectors were held by a small disk with a threaded shaft fixed in the center. This shaft screwed through an arm which was affixed to the target holder. Figure 4-2 shows the target holders. Figure 4-3 shows the detail of the collector holder. The physical size of the holding arm is shown in Figure 4-4 and a schematic of the target-collector set is shown in Figure 4-5.

4. Scanning Electron Microscope

The Scanning Electron Microscope used in this thesis was a Stereoscan S4-10 scanning electron microscope. It enabled the examination of a surface whose roughness or other characteristics render their observation extremely difficult or impossible by means of a conventional Transmission Electron Microscope. The Stereoscan has a direct reading magnification system which provides a useful range between X20 and X100,000, corresponding to scanned areas of 5 mm to 2 μ m square on the specimen. The standard specimen stage allows objects of up to 12 mm in diameter and several millimeters thick to be manipulated in any required

orientation under observation. A detailed description is presented in Appendix B.

5. PGT Microanalysis System

The Basic PGT Microanalysis system consists of a lithium drifted silicon detector, a low noise preamplifier, a linear amplifier, a detector bias supply and the PGT-1000 x-ray analyzer [28]. It is possible to perform chemical analysis simultaneously for elements from Fluorine ($Z = 9$) to Uranium ($Z = 92$) under a rapid and nondestructive materials analysis. The microanalysis system gives the scanning electron microscope many of the capabilities of a microprobe, without the disadvantage of high beam currents which causes sample changes. The block diagram of this system is shown in Figure 4-6.

6. Optical Microscope

In the experiments, the Bausch and Lomb Dynazoom Metallograph was also used. This system is constructed on the reverted microscope principle. It has a rotatable glide stage, quadruple rotosphere nosepiece, and a highly corrected optical system. Applications for a dark field and for polarized light are also possible by using Dynazoom body styles. The quadruple nosepiece is movable for centering and rotating the objectives. Magnifications range from X50 to X800. This system fits several kinds of cameras, but most commonly used are a 35 mm camera and a Polaroid camera. A detailed description of the operation is given by reference [29].

B. PROCEDURES

1. Surface Damage Studies

A thin, roughly polished target, was weighed and the weight recorded. It was then affixed to the target holder which was mounted in the vacuum chamber. The entire system was evacuated to a pressure of about 10^{-6} Torr. This pressure was achieved after about three hours of evacuation time. Before data were taken, all gauges, meters and oscilloscopes were calibrated.

The charging power supply voltages were set so that the laser output energy was about 5 Joules. The He-Ne alignment laser was turned on and adjusted to insure that the laser light was focused through the lens at the right position on the target. This lens had a 30 cm focal length and was able to focus the beam to a tiny point. The laser was fired and the energy was recorded.

Ten different experiments were undertaken in this surface damage study. Although the laser output remained at approximately 5 Joules, the different experiments consisted of several 5 joule shots onto the same target. Therefore, integration of the energy of these 5 joules outputs resulted in a different total laser energy deposited on the targets. After each experiment the chamber was opened and the target was taken out and reweighed. These procedures were repeated until all the targets had been shot and weighed.

The targets were analyzed using an optical microscope with a magnification of X100. Photographs revealed the area of the damaged hole. In order to measure the depth of the damaged hole the optical microscope, with a magnification of X400, was focused on a portion of the undamaged surface and the number from the focus adjusting nob was recorded. Then the specimen was repositioned and the microscope was focused on the bottom of the laser drilled hole. The associated number from the focus adjusting nob was recorded. The difference between these two focusing numbers determined the depth of the damaged hole.

2. Studies of Deposits on Collector

A thick, well polished target was affixed to the target holder. A well polished, thick stainless steel collector, with its surface half blocked, was fixed on the collector holder which was threaded through the holding arm (see Figure 4-5). The arm was then fixed on the target holder. This whole assembly was then set in the chamber and evacuated to a pressure of about 10^{-6} Torr. Several shots were necessary in order to have enough evaporated material deposited on the collector. After the evaporation experiments were finished, the target and the collector were sealed separately on the aluminum stub by using silver paint. This procedure allowed the specimen to be analyzed by the scanning electron microscope.

Then, the target stub was put in the assembly column chamber of the SEM. It was analyzed and photographed

with different magnifications over the different areas. The collector stub was also analyzed and photographed on both the evaporated surface and the unevaporated surface with high magnification.

Another experiment used aluminum stubs as collectors instead of using thick stainless steel disks. After laser irradiation of the targets, the aluminum collectors were put in the assembly column chamber of SEM. This sample was scanned and analyzed by the PGT 1000 x-ray analyzer. Both the unevaporated surface and the evaporated surface were analyzed and photographed using this technique.

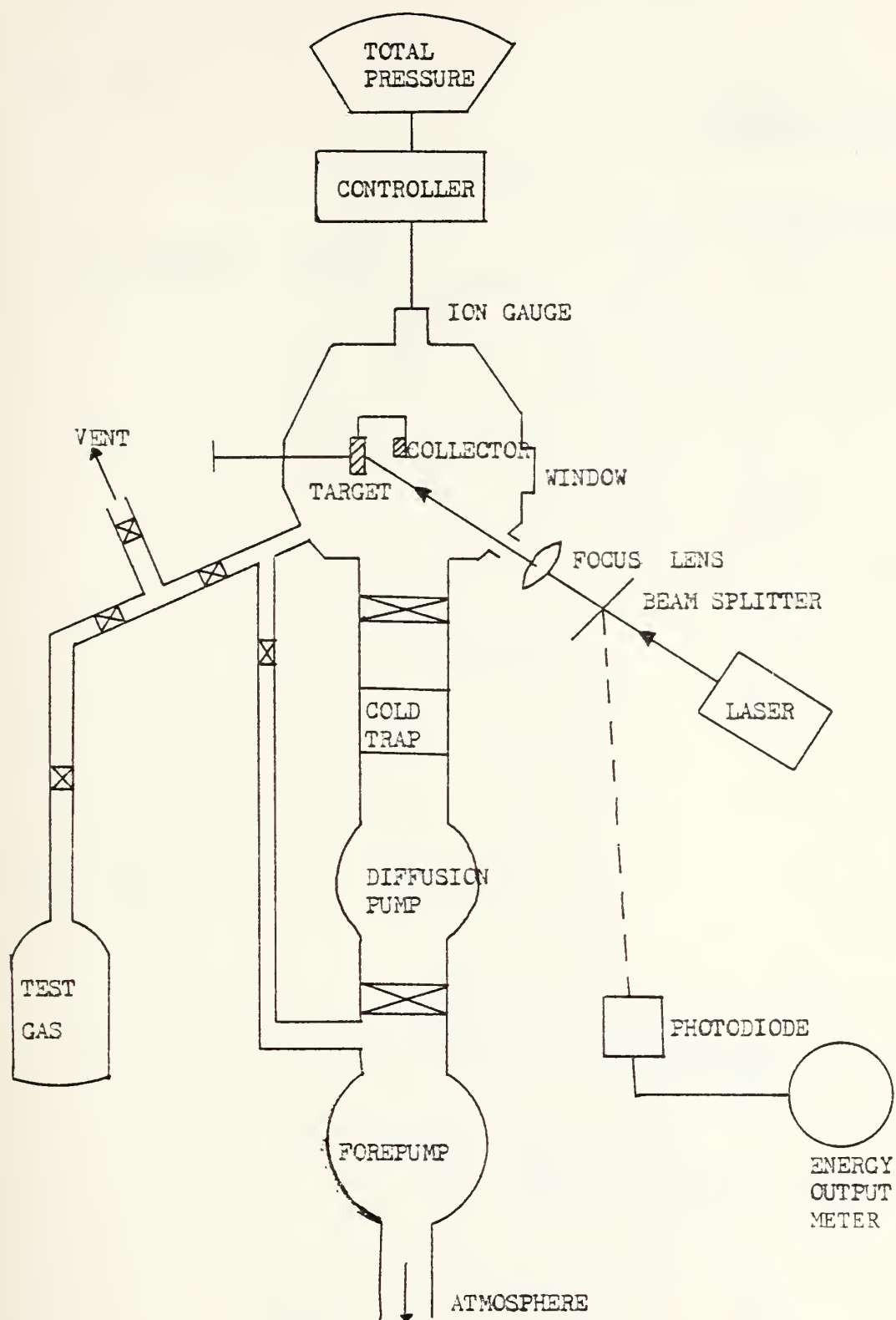
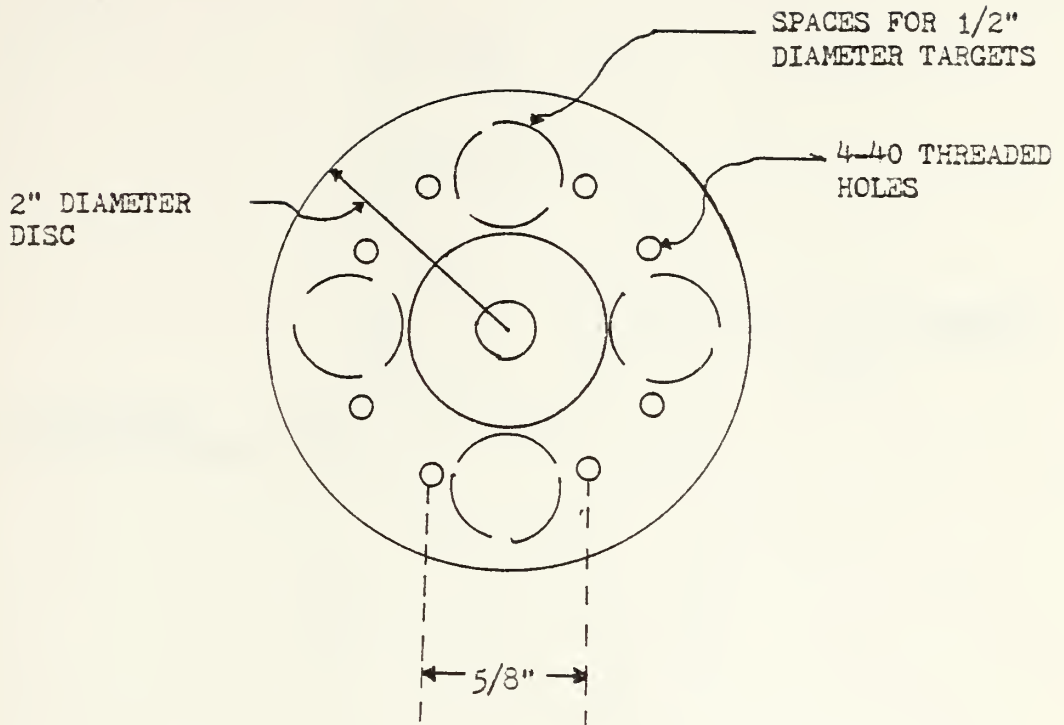


Fig. 4-1 Schematic of experimental arrangement

TOP VIEW



SIDE VIEW

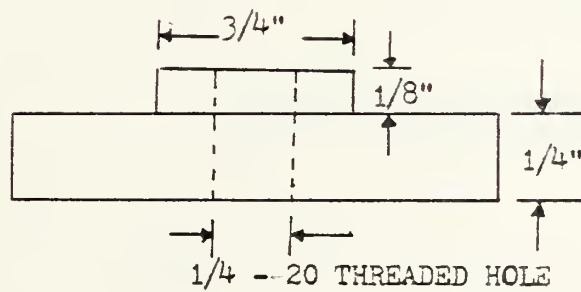
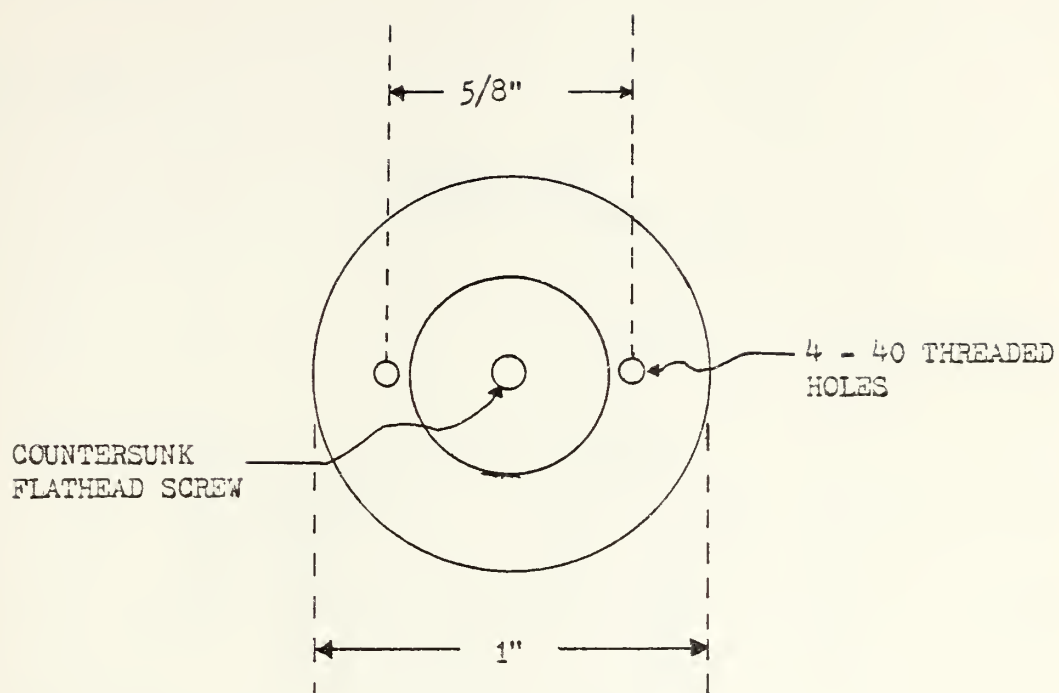


Fig. 4-2 Target holder

TOP VIEW



SIDE VIEW

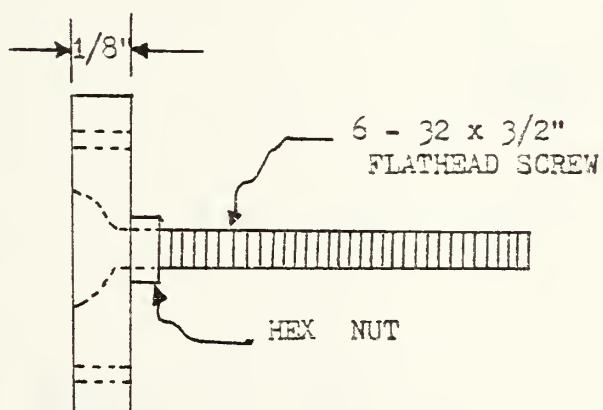
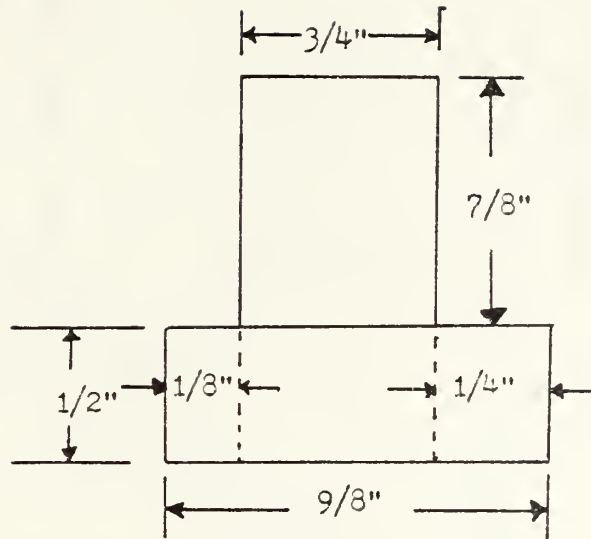


Fig. 4-3 Collector holder

TOP VIEW



SIDE VIEW

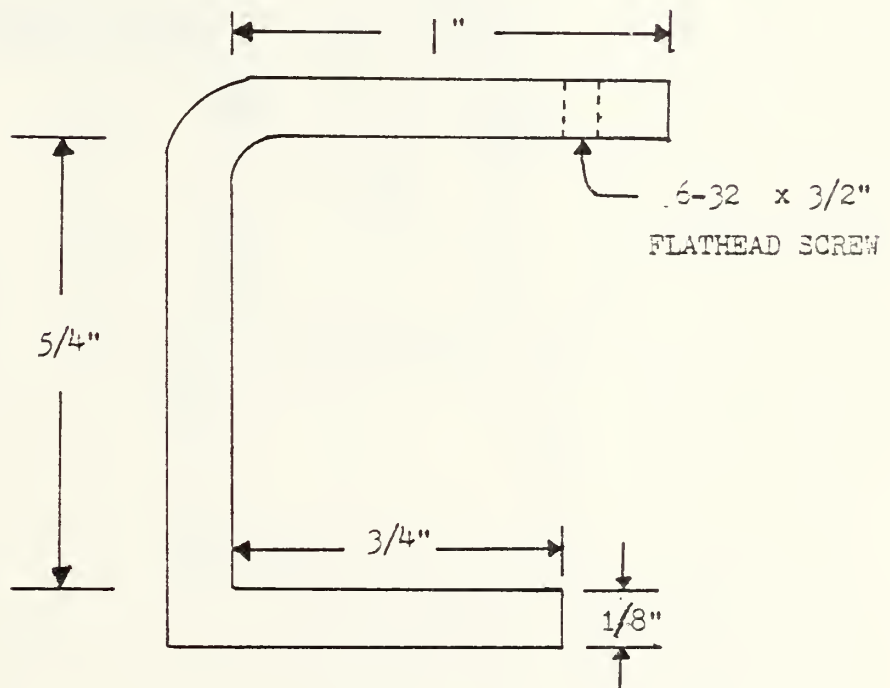


Fig. 4-4 Holding arm

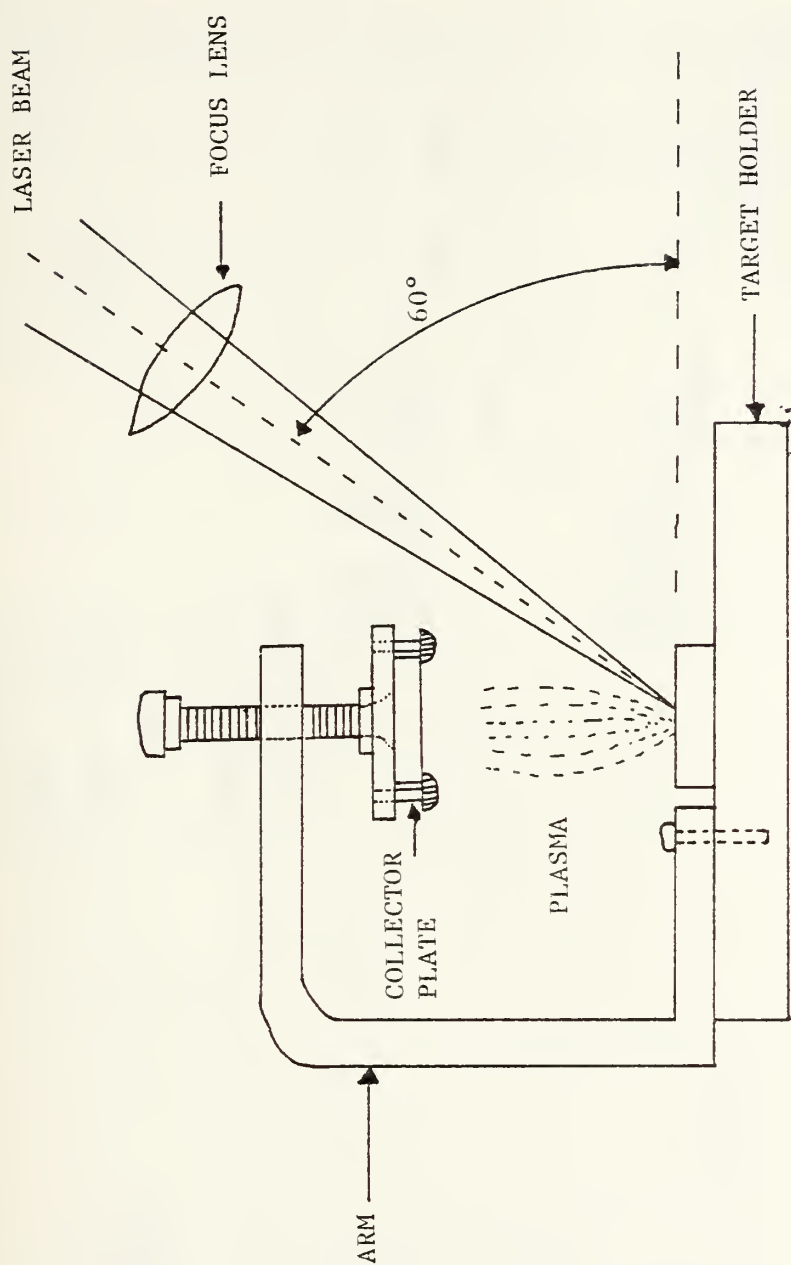


Fig. 4-5. Target and collector arrangement

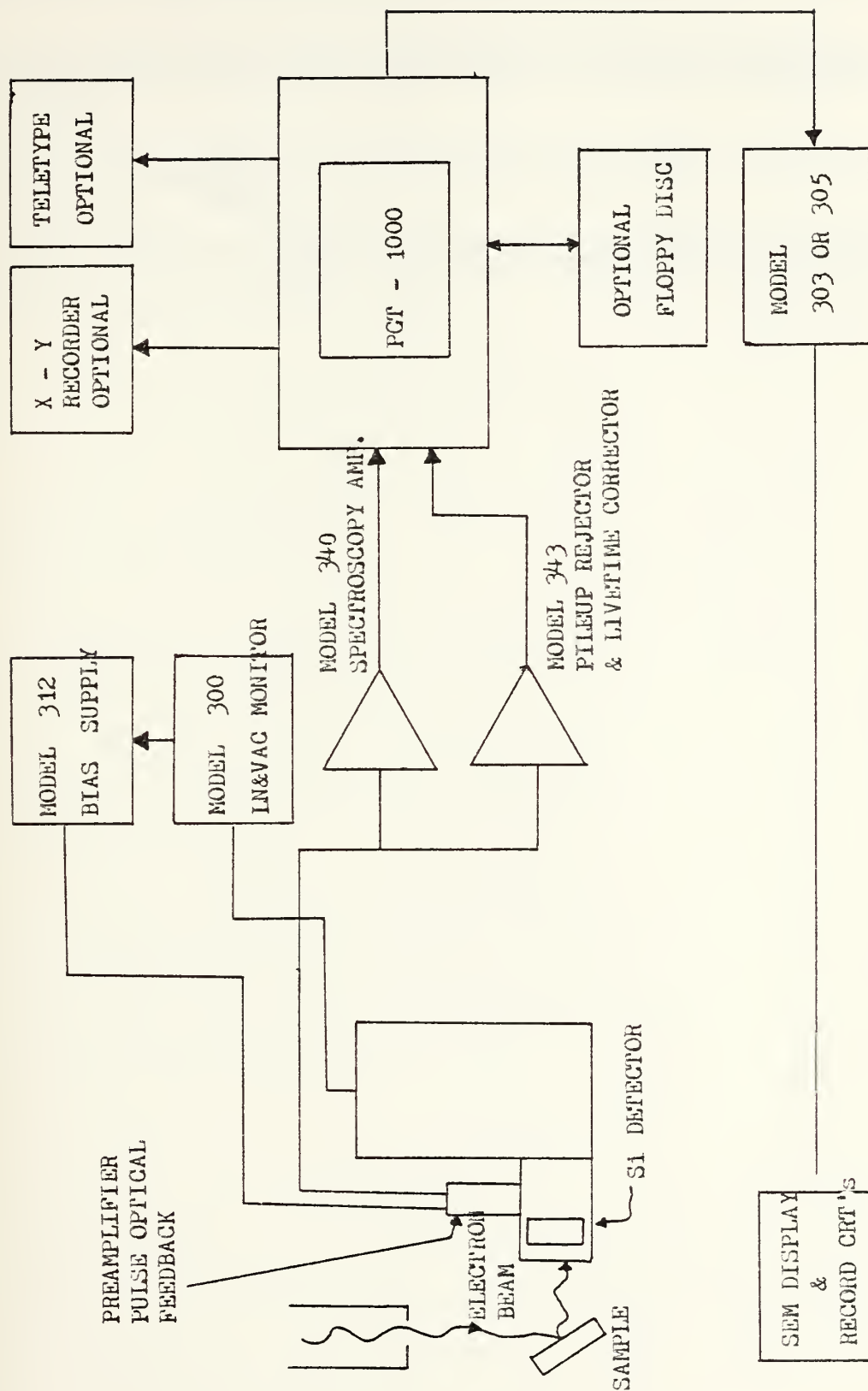


Fig. 4-6 Basic PGT Microanalysis System

V. RESULTS AND DISCUSSION

Laser-induced evaporation from the metal surface was easy to document by taking a photograph when the interaction process happened. Figure 5-1 shows the evaporated materials emitted from the metal surface upon interaction with the laser pulse. This photograph was taken without any background light. The visible light is due only to plasma formation. The plasma expands in the direction normal to the metal surface and then fills finally all of the chamber. The evaporated materials were collected in front of the metal target. Figure 5-2 shows the mechanism which allows the evaporated materials to be collected.

A. COMPARISON OF SURFACE DAMAGED BY ONE SHOT WITH CERTAIN LASER ENERGY TO THE SURFACE DAMAGED BY THE SAME AMOUNT OF ENERGY INTEGRATED OVER SEVERAL SMALL ENERGY SHOTS

The mass measurement instrument used in the experiment was significant only to 10^{-4} grams. Because of the limitation of available laser power and the limitation of the mass measurement instrument, several laser shots were needed to remove a measurable amount of mass. For this reason, a comparison between one shot with a certain laser energy and several shots with small energies integrated to the same amount of energy was absolutely necessary. For example, in the case of one shot with 3.9 J compared to 10 shots with each shot of 0.4 J, results showed the depth of damaged hole from a stainless steel surface with only one

shot was less than the depth from 10 shots. Also, the area of the damaged hole showed a similar behavior. The mass evaporated was mostly determined by the depth and the area of the laser drilled hole. It was observed that the mass evaporated from a stainless steel surface as a result of one laser pulse was less than the mass evaporated by several small laser pulses integrated to the same amount of energy. This is due to the fact that high irradiance shot is higher than the optimum laser intensity. This effect agrees with the results of reference [12]. Nevertheless, the total damaged area (not only the hole) of the metal surface caused by only one giant laser pulse was larger than the total damaged area for the case of several shots. This is due to the larger radial expansion of the hotter and denser plasma produced by the higher power laser pulse. Figure 5-3 shows this phenomenon.

B. MASS OF EVAPORATION

The laser power densities in the experiment were in the range of 10^9 to 10^{10} Watt/cm². These densities were in the range of CARUSO's model. Therefore, the experimental results were used to compare with the expected solutions calculated according to CARUSO's model.

The mass of evaporation was found to be proportional to the laser power density. This is plotted in a log-log scale in Figure 5-4. The dotted line shows the linear regression line from the data taken in the experiment.

The correlation coefficient is 0.984 and the slope equals 0.479. In the same plot, the calculated line is also shown. The solid line is calculated from equation (3-6) for a one shot laser pulse of certain flux density. Using an atomic number of stainless steel equal to 56, then a, the constant which appears in equation (3-6), was calculated to be 2.65×10^{29} . The laser pulse width, t , was equal to 25×10^{-9} sec. The slope of the solid line is equal to 0.5. Comparing the experimental result to the calculated result in CARUSO's model, it can be seen that the slopes are in agreement with each other. The mass of evaporation was approximately proportional to $F^{1/2}$ where F is the flux density in W/cm^2 . However, the amount of mass evaporated in the experiment was about one order of magnitude greater than the amount of mass calculated by equation (3-6). See Figure 5-4.

This result can be interpreted from the results presented in part A of this section. One assumed the power density was additive. For example, $8 \times 10^{11} \text{ Watt/cm}^2$ was obtained by shooting 40 shots with each shot equal to 5 Joules over a spot area of 10^{-2} cm^2 . But from the results of part A of this section, it was shown that the mass evaporates due to 40 shots with each shot equal to 5 Joules was larger than the mass evaporated by only one shot with $8 \times 10^{11} \text{ W/cm}^2$. This is due to reduced momentum transfer at the higher laser irradiance. Also, with several shots a

"softening" of the crystal structure of the target material may occur due to the repetitive heat and shock waves transmitted.

C. DEPTH OF DAMAGED HOLE

The depth of the damaged hole was measured by looking at the bottom of the hole and the undamaged surface with an optical microscope. This difference between these two focal distances was the depth of the hole. The results showed that the depth of the damaged hole was proportional to the laser power density. This result has been plotted in a log-log scale in figure 5-5. The correlation coefficient is 0.9978 and the slope is equal to 0.832. This shows that the depth of the damaged hole is approximately proportional to $F^{0.8}$, where F is the laser flux density in W/cm^2 .

D. AREA OF DAMAGED HOLE

The area of the damaged hole was measured from a metallograph taken with an optical microscope. One measured the area of the magnified, damaged hole, and then calculated the actual value of area. Results showed that the area of the damaged hole was proportional to the laser power density. This relation is plotted in a log-log scale in figure 5-6. The correlation coefficient is 0.987 and the slope is 0.692. This shows that the area of the damaged hole is approximately proportional to $F^{0.7}$, where F is the laser flux density

in W/cm². One difficulty encountered was that the shape of the damaged area was not easily recognized if the laser irradiance was too small. Also, the laser beam was not completely Gaussian in shape. This actually caused the most difficulty in determining the area of the damaged hole.

E. METALLOGRAPH OF DAMAGED SURFACE

Laser-induced damage to the metallic surface was analyzed by metallographic methods. Some results of the metallograph were analyzed by an optical microscope, some by the scanning electron microscope. Because of the different characteristics of these two microscopes, it was an advantage to use the SEM in most cases. In other cases, it was an advantage to use the optical microscope. For example, the SEM can see a bigger area than the optical microscope can do using the same magnification.

A stainless steel surface after irradiation by 40 shots of the laser was analyzed. The entire surface was scanned in the SEM screen and it was found that there were several distinctive places that merited further investigation. The entire damaged surface included the hole at the center, the bottom of the hole, and three zones with different kinds of damage patterns. Figure 5-7 to Figure 5-11 shows these phenomena. Figure 5-7 shows the hole in the center and an associated wave pattern surrounding it. The wave length became smaller as it propagated farther from the hole.

Finally, it reached the interface between the two different damage zones, as seen in figure 5-10, as a section of a smooth band. The radius of the inner zone measured from the center of the damage area produced by 40 shots of laser pulse is 1.4 mm, while the radius of the outer zone is 2.2 mm. From the figure it is clear that two kinds of damage patterns exist.

Figures 5-12 to figure 5-19 show the details from the edges of the hole, produced by 40 shots of about 5 joules each, out to the undamaged surface. If each photograph were connected from left to right, the entire damaged surface would be clearly presented. The outer zone was not heavily damaged because most of the laser energy was distributed in the center of the beam. The damage to the outer zone is due to the interaction of the radially expanding laser produced plasma with the surface. In figures 18 and 19 very clearly visible are small craters in the outer zone. These small craters are probably caused by small arcs between the plasma and the surface.

Figures 5-20 to 5-23 show the detail of each portion of a stainless steel when only one shot of 3 J of laser energy was absorbed. In this case, there were no two distinct inner zones observed. The wave structure on the surface existed only at the edges of the hole. The remainder of the target surface was damaged of the same kind that the outer zone was damaged after irradiance of 40 shots of the

laser pulses. The size of the arc craters become smaller with increasing distance from the focal spot. Also, noticable is the asymmetry in the crater rim, figure 5-22. The craters are of horse shoe form and open in radially increasing direction.

F. ANALYSIS OF COLLECTOR SURFACE

Analysis of the collector surface proved the validity of laser-induced evaporation. This had been done in two different ways. One was metallographic analysis of the collector by using the SEM. The other method was mass spectrum analysis of the collector by using the PGT 1000 x-ray analyzer. The deposition of vaporized materials involved the mechanism of plasma-wall interaction. The position at which the collector was located was also important. The collector had to be located so that it was not in the way of the reflected laser beam. Otherwise, it would not only not collect vaporized material but also the collector surface would be damaged. Therefore, the deposition of evaporated material depended upon many factors.

Figures 5-24 to 5-28 show the results analyzed from a polished stainless steel collector. Figure 5-24 shows the unevaporated surface without any deposition. In other words, it was the collecting background. Figure 5-25 shows some small particles in the exposed portion after 40 shots. These particles were deposited as a result of laser vaporization of the target material. Under the same

evaporation condition, the degree of deposit was assumed to be proportional to the number of shots. The average distance between particles was measured to be 10^{-4} cm. There were many small particles that could be resolved in the photograph. Figure 5-26 is the enlargement of some particular particles used to measure the size of particles. The largest particle in the figure was measured to be about 3800 \AA in diameter. This only indicated some idea of the particle sizes under this magnification. Because of the limitation to available magnification, it was impossible to see the smallest particles.

Figure 5-27 shows the particles in the exposed portion after 20 shots. The particles that could be resolved were farther apart than those in figure 5-25. The average separation between particles in figure 5-27 was 4×10^{-4} cm. From figure 5-28 the particle diameter was measured to be 3220 \AA .

The PGT 1000 x-ray analyzer showed the relative amount of elements from atomic number 9 through atomic number 92. Figure 5-29 shows the background spectrum of an aluminum surface. The largest peak evident was Al/13. The peak on the right most side was Cu/29. The cursor was located on some position and the keys, ELEMENT and ENTER, were pushed. It would show the element indicated. Figure 5-30 shows Fe/26 as an element and figure 5-31 shows the element Cr/24. After comparing the relative amount of Fe/26 to the

relative amount of Cr/24, it was clear that the line of the element Fe/26 was higher than the line of the element Cr/24. This was correct because 304 stainless steel contains 71% Fe/26 and 18% Cr/24. The other elements were too small to be detected.



Fig. 5-1. Evaporated material expanding from the target surface

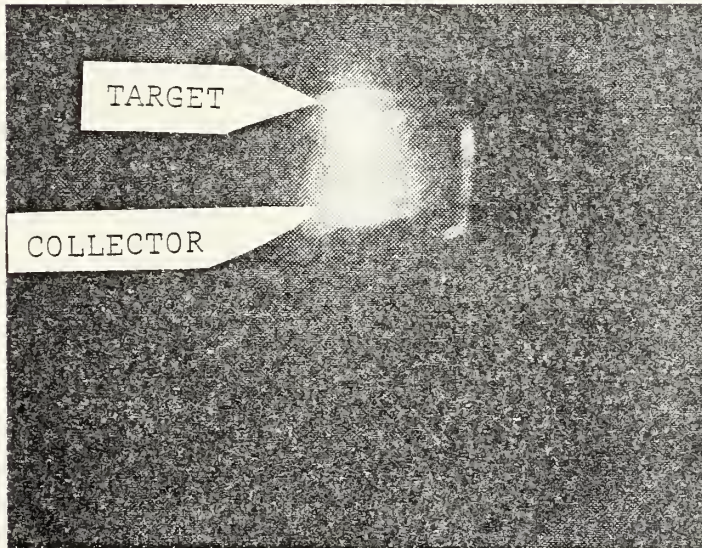


Fig. 5-2. Evaporated material depositing on the collector

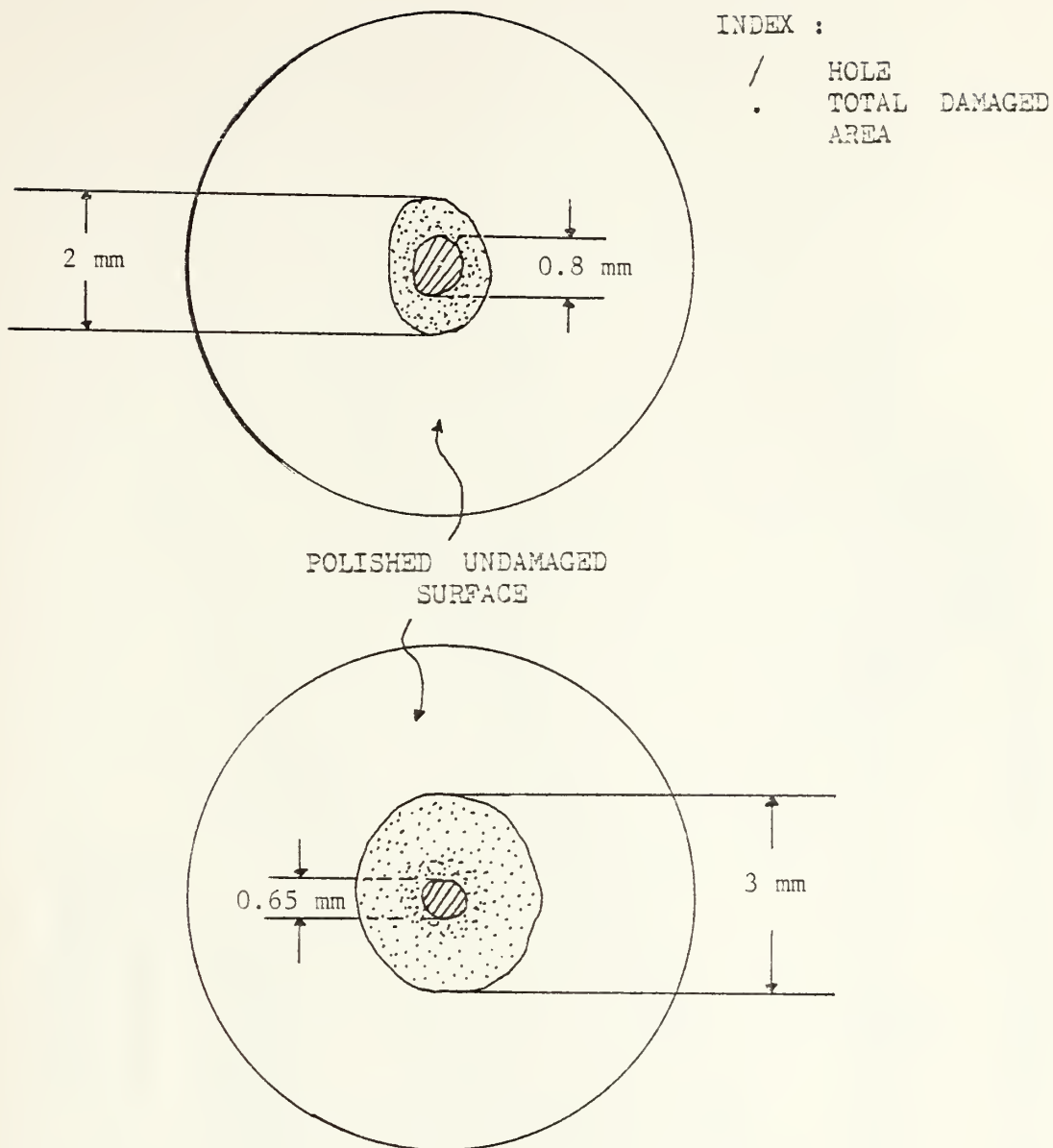


Fig. 5-3. Comparison of two damaged surfaces. Bottom one was damaged by only one giant laser pulse of 3.9 J, top one by 10 shots of 0.4 J each that the total deposited energy is approximately the same as for one giant pulse. Total damaged area of the bottom surface was larger than total damaged area of the top surface. But the area of hole of bottom surface was smaller than the area of hole of top surface.

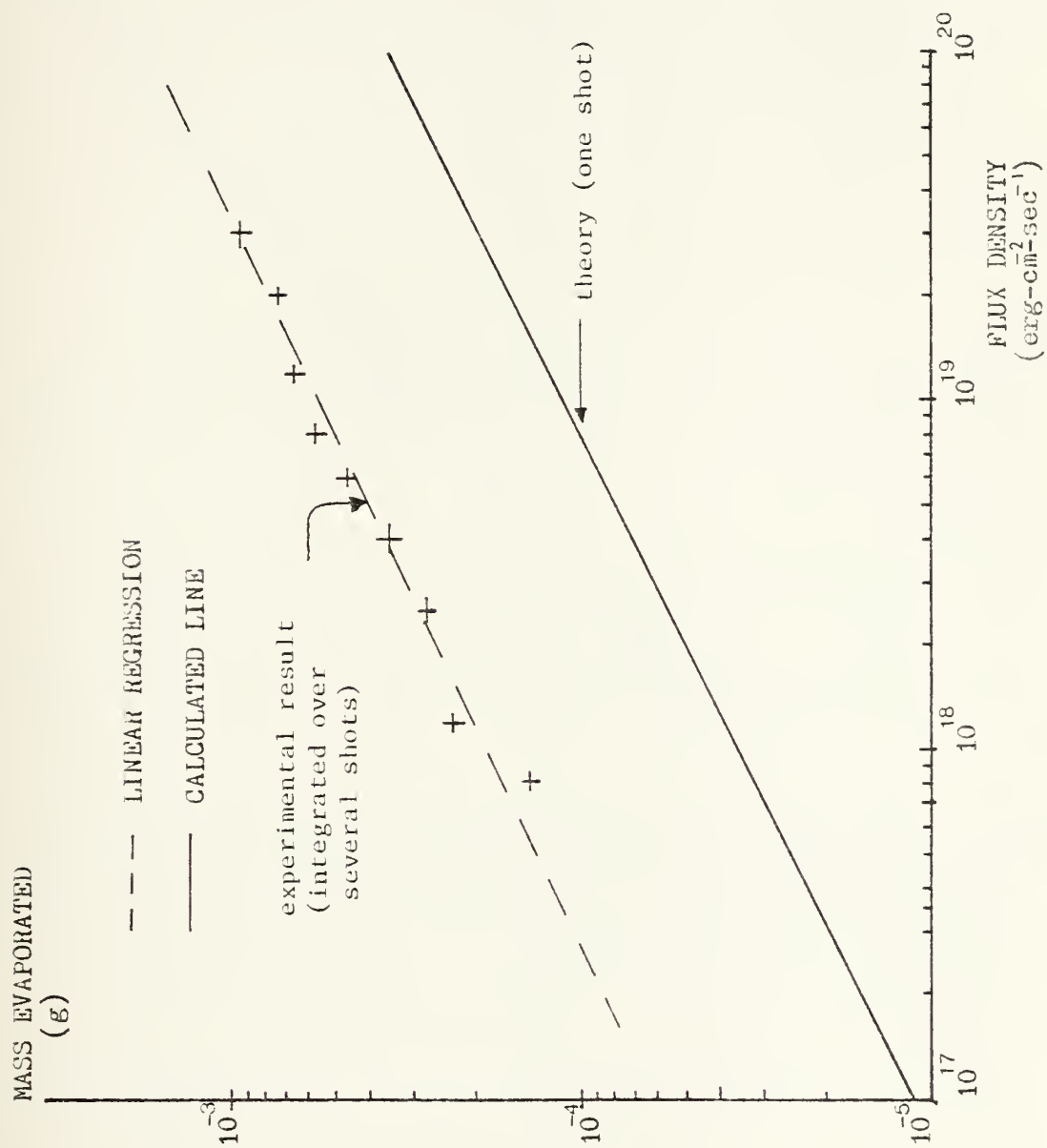


Fig. 5-4 Mass evaporated from stainless steel surface

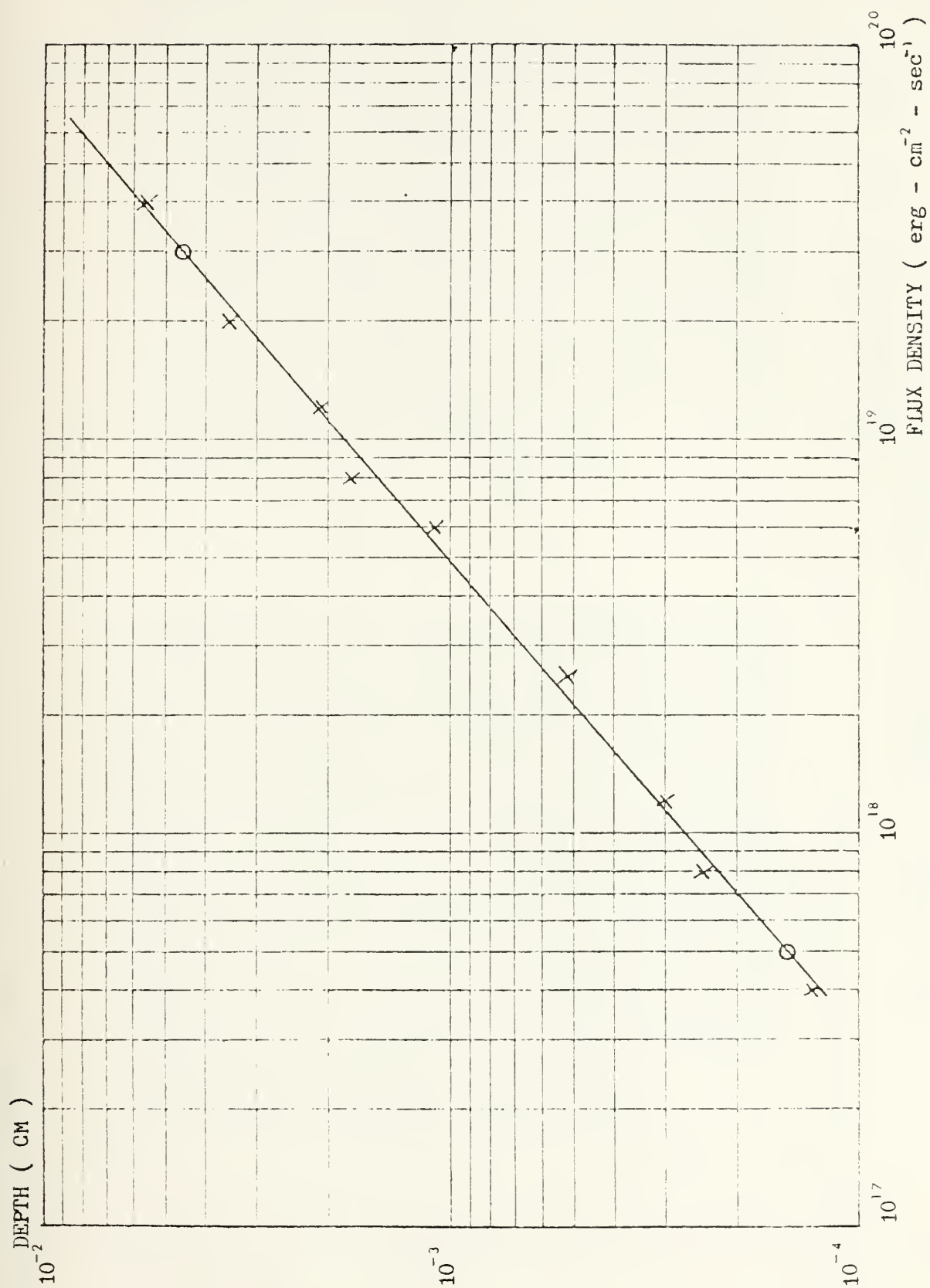


Fig. 5-5 Depth of damaged hole as a function of flux density

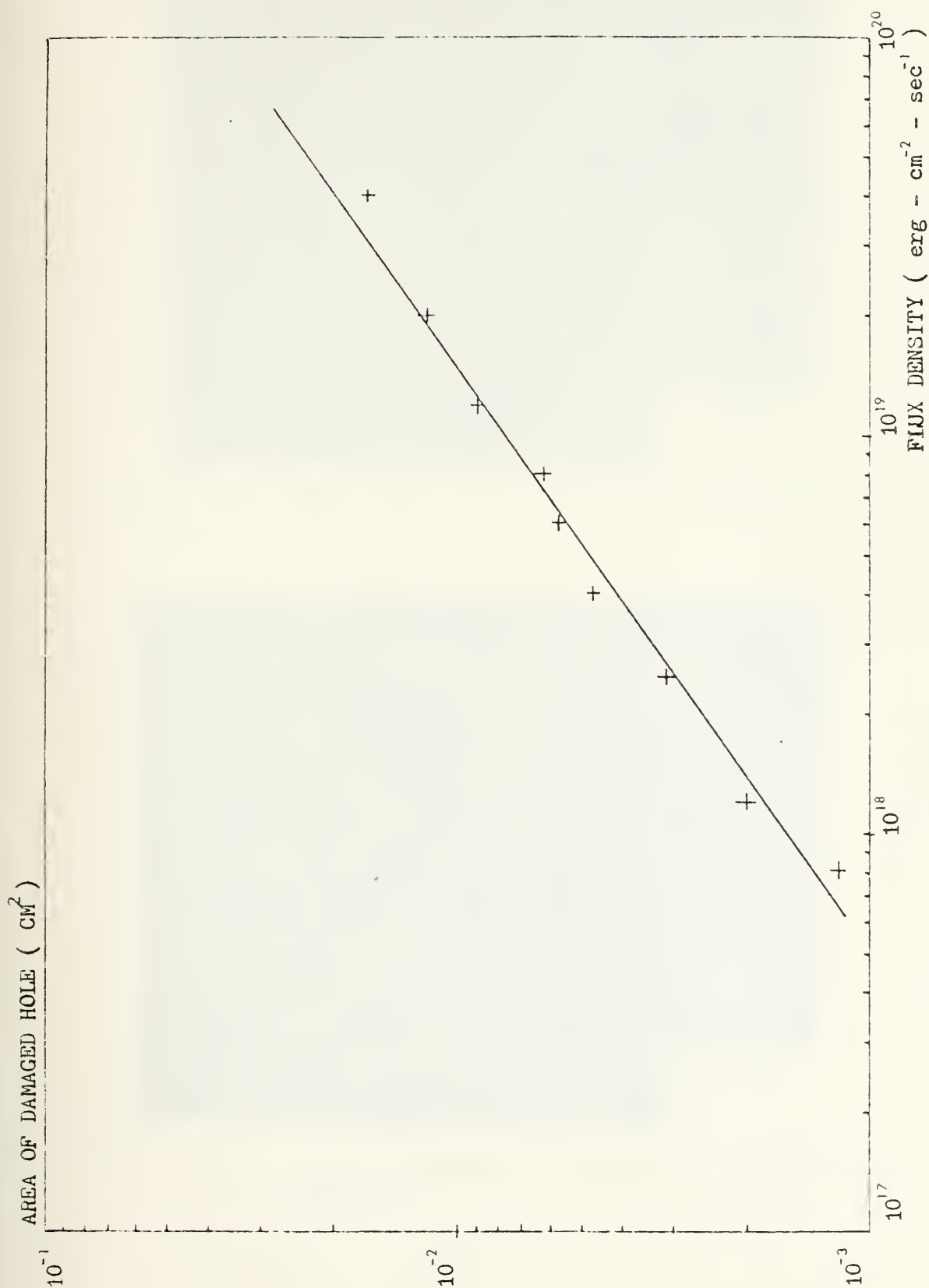


Fig. 5-6 Area of damaged hole as a function of flux density

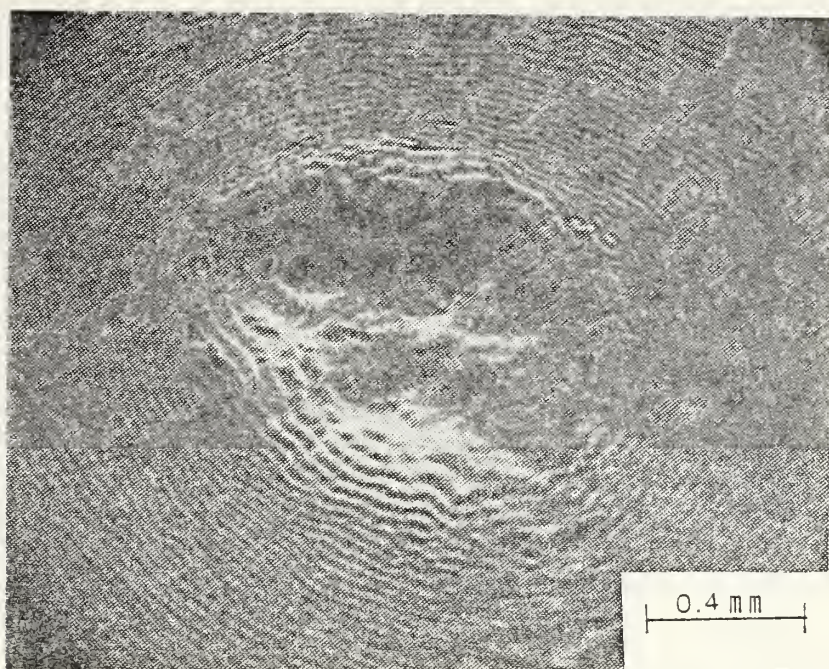


Fig. 5-7. Whole area of the damaged surface (40 shots)

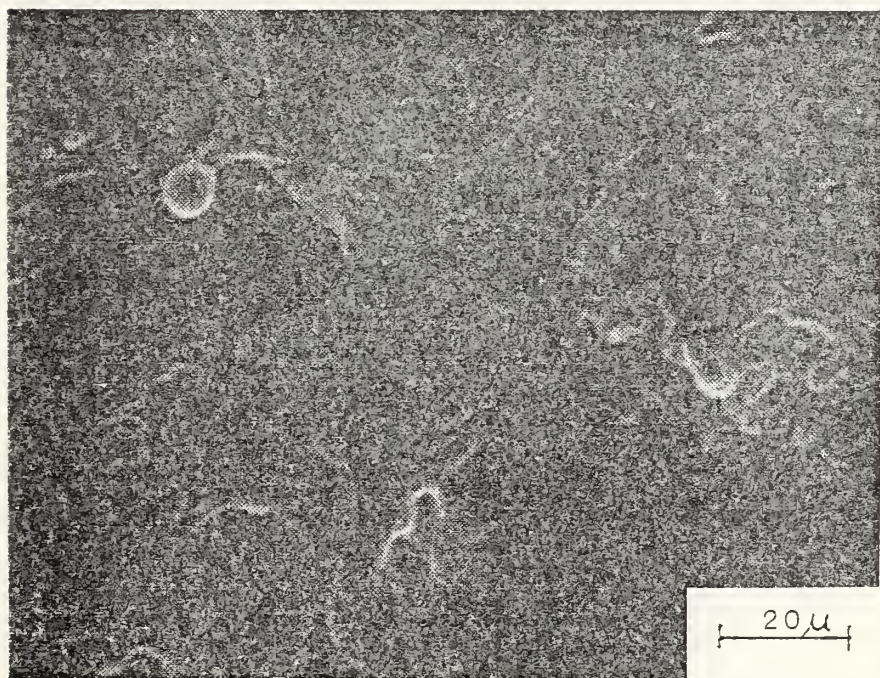


Fig. 5-8. Damaged phenomenon of the bottom of the hole (40 shots)

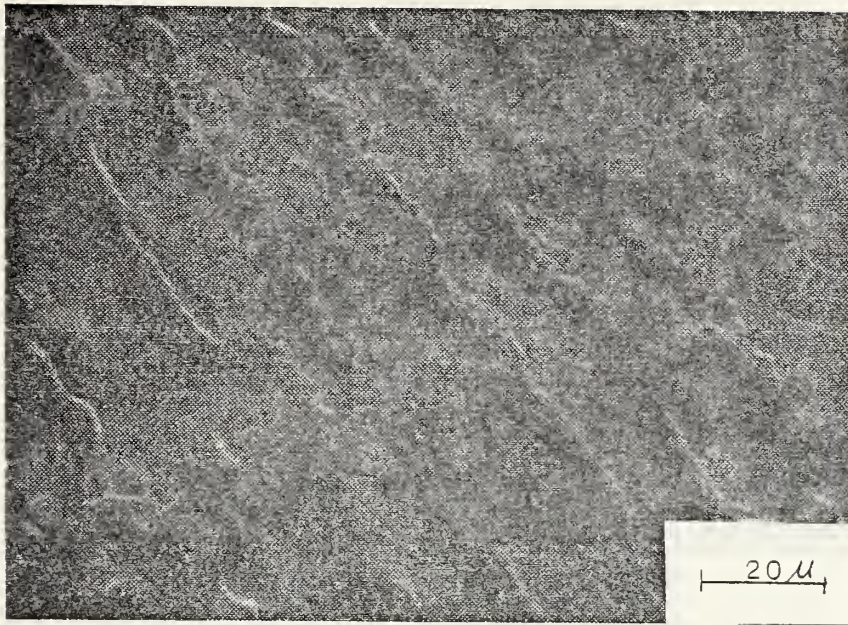


Fig. 5-9. Wave shaped damaged surface of inner zone (40 shots)

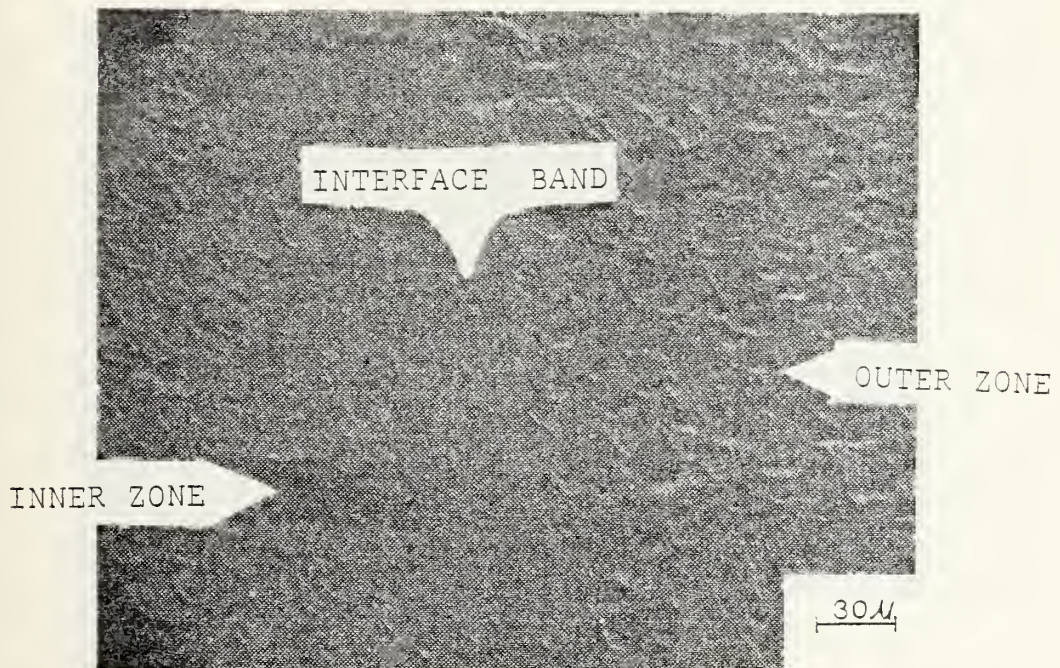


Fig. 5-10. Damaged phenomena of interface of zones (40 shots)

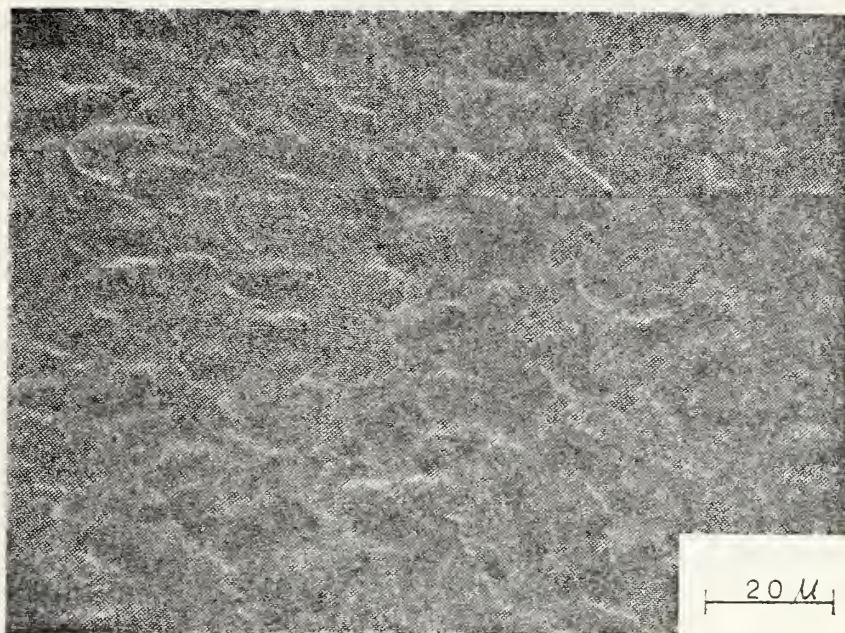


Fig. 5-11. Irregularly damaged surface of outer zone
(40 shots)



Fig. 5-12. Surface around the edges of the damaged hole
(40 shots)

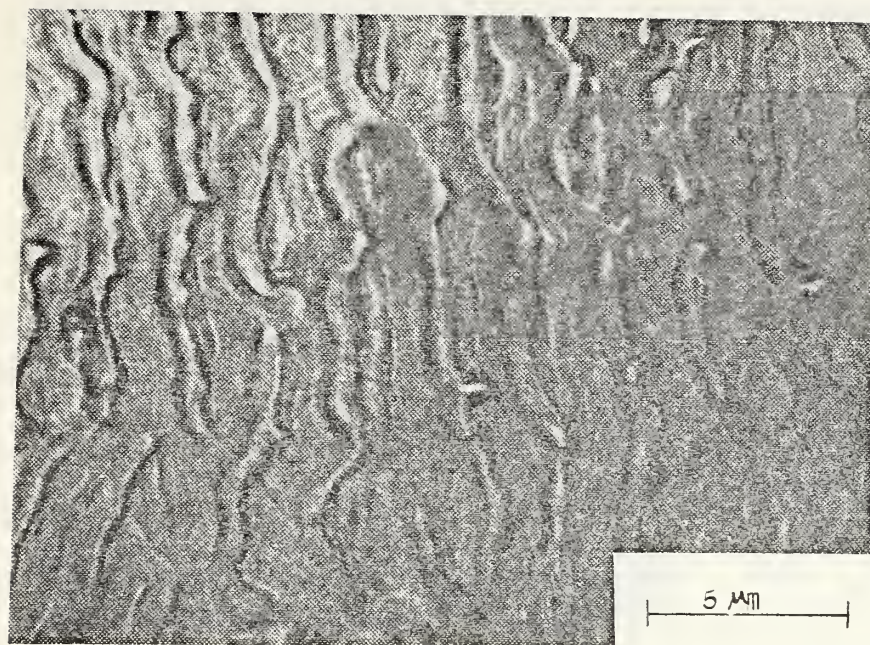


Fig. 5-13. Wave shaped damaged surface of inner zone propagated from left to right (40 shots)

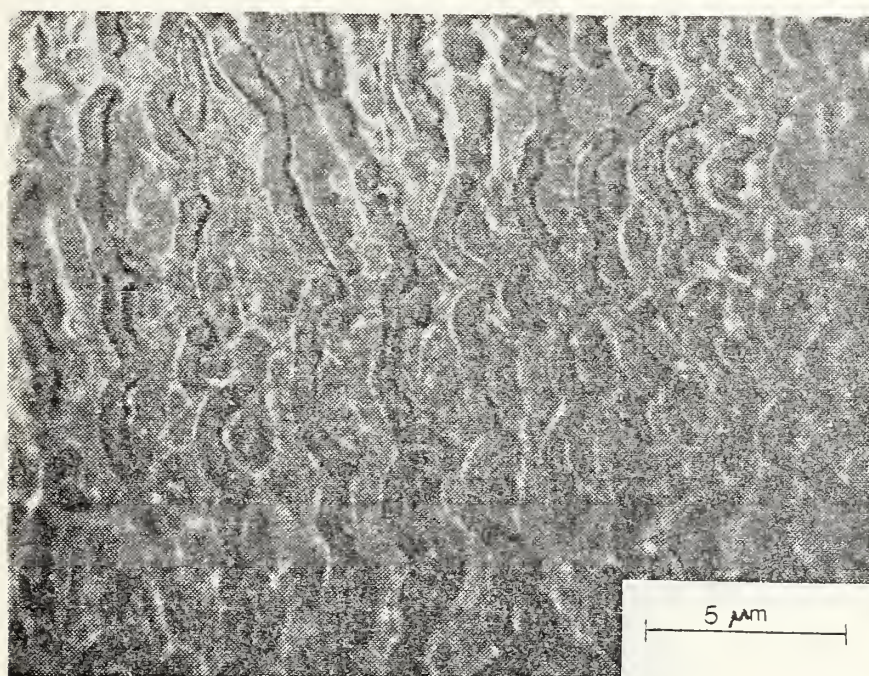


Fig. 5-14. Wave shaped damaged surface propagated farther out of inner zone (40 shots)

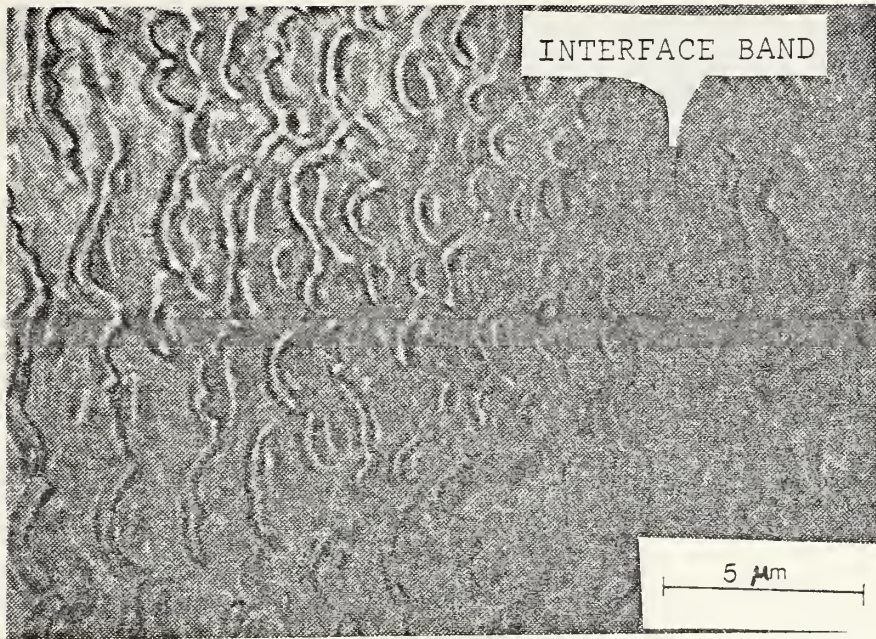


Fig. 5-15. Wave shaped damaged surface near interface of zones (40 shots)

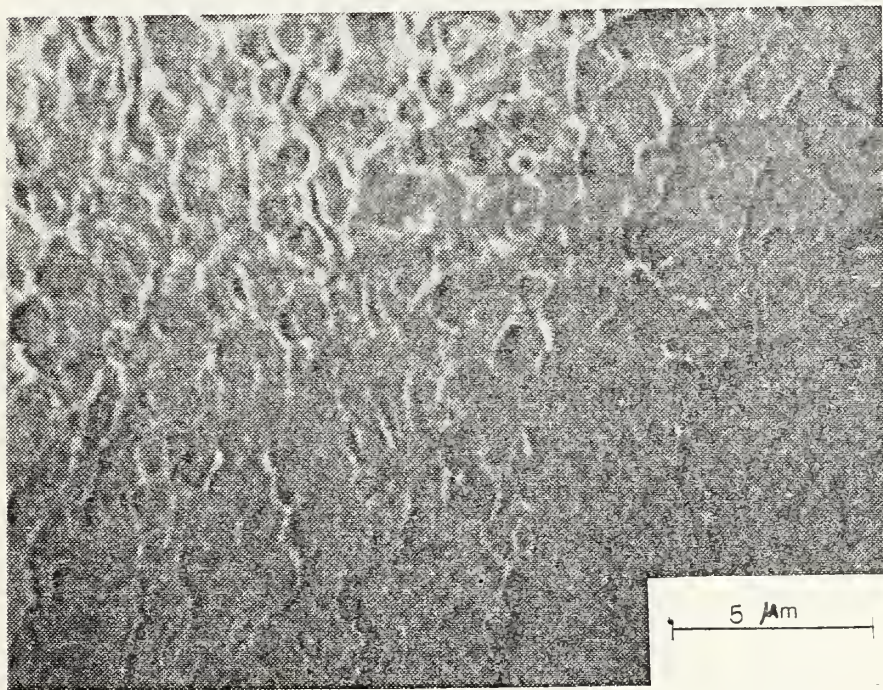


Fig. 5-16. Irregularly damaged surface near interface of zones (40 shots)

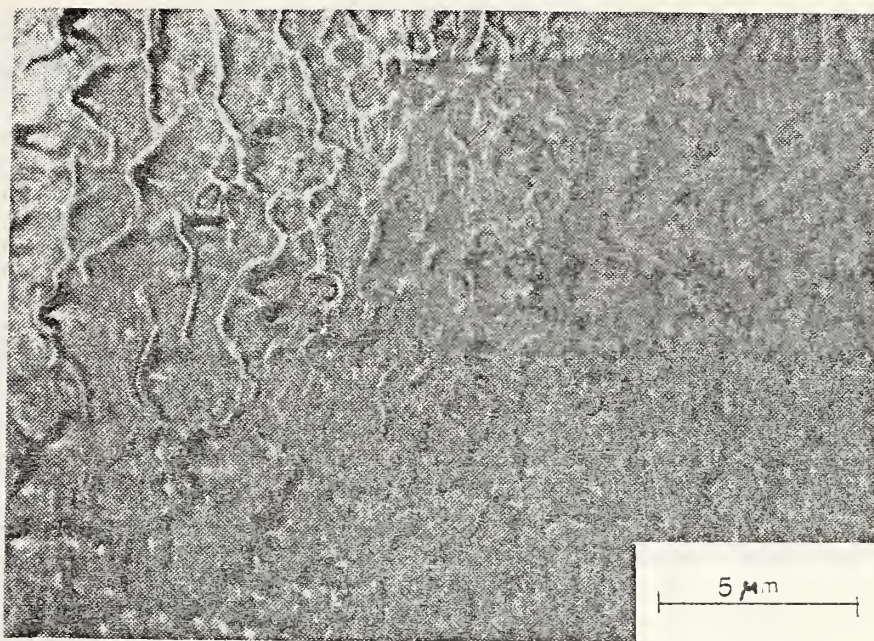


Fig. 5-17. Irregularly damaged surface of outer zone (40 shots)

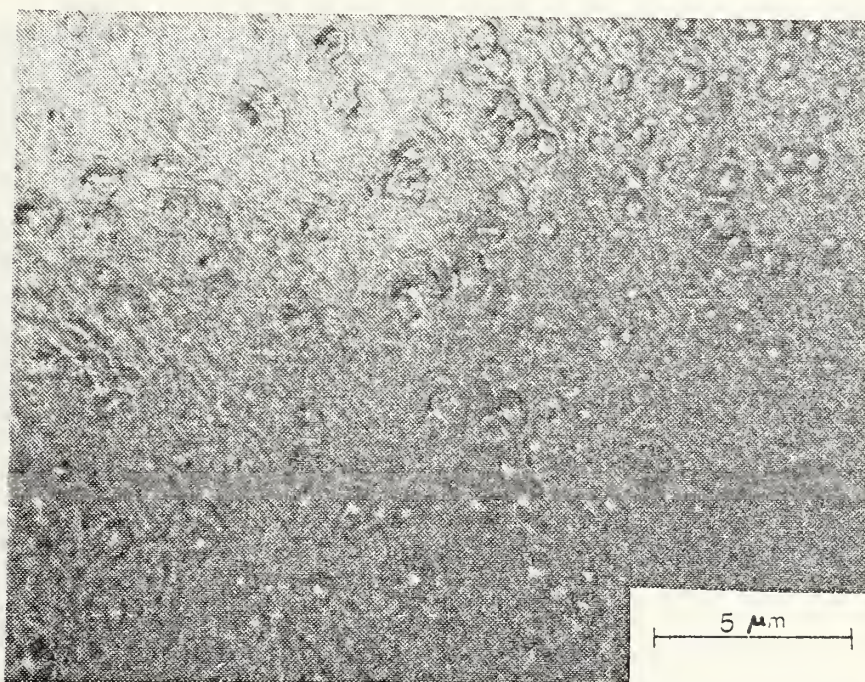


Fig. 5-18. Irregularly damaged surface farther out of outer zone (40 shots)

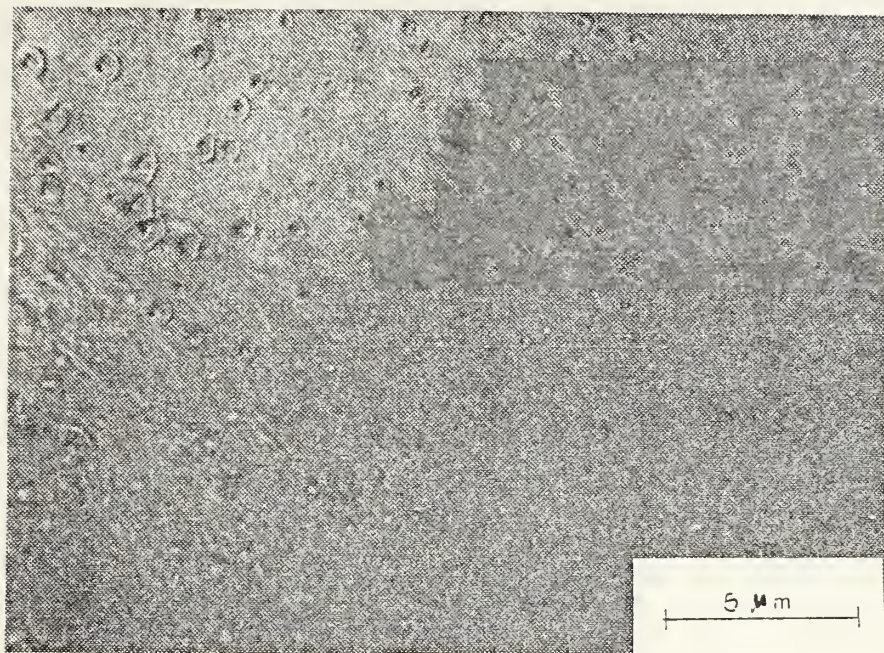


Fig. 5-19. Interface of outer zone and undamaged surface (40 shots)

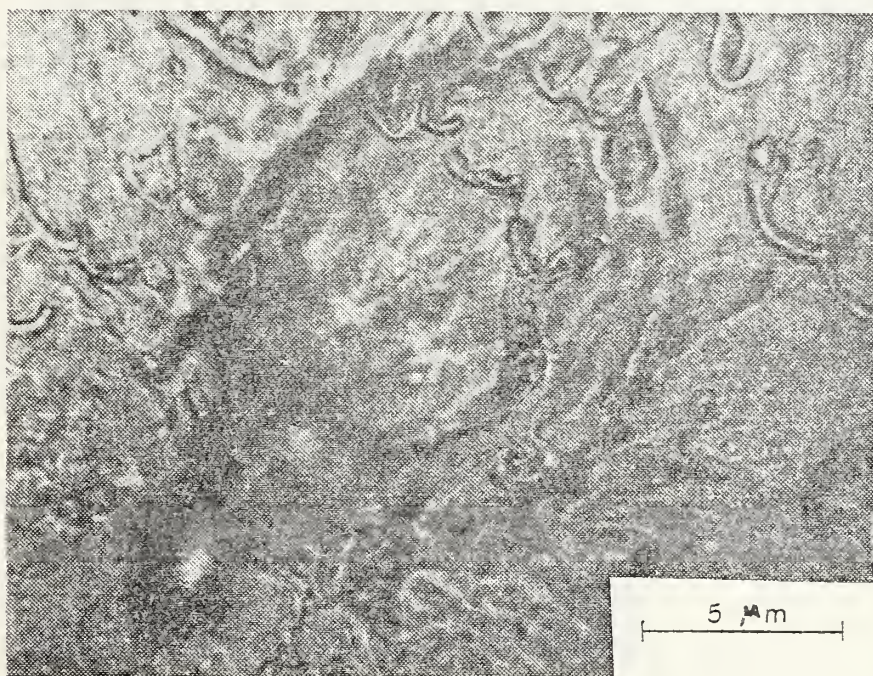


Fig. 5-20. The damaged hole shot by 3 J laser energy (1 shot)

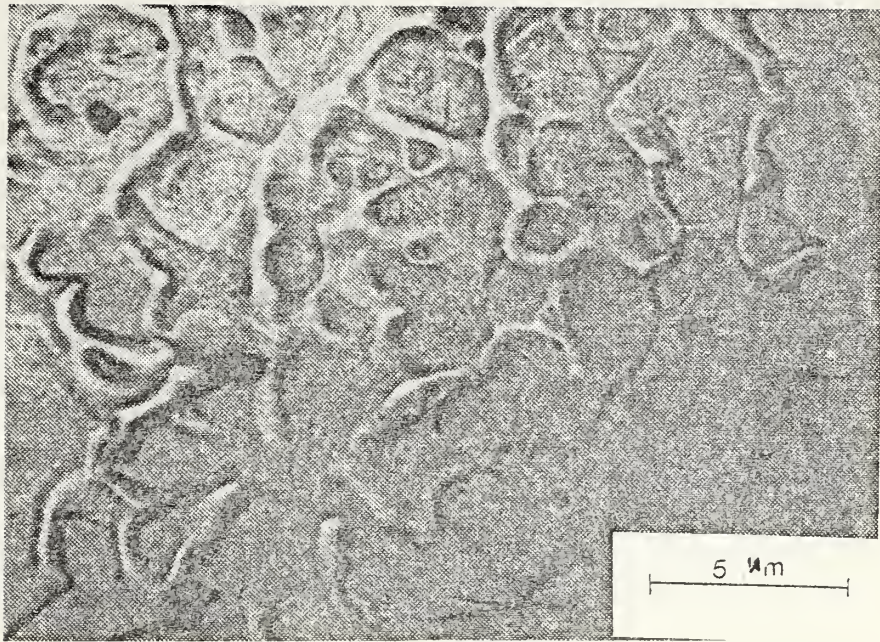


Fig. 5-21. Edges around the damaged hole by 3 J laser energy (1 shot)

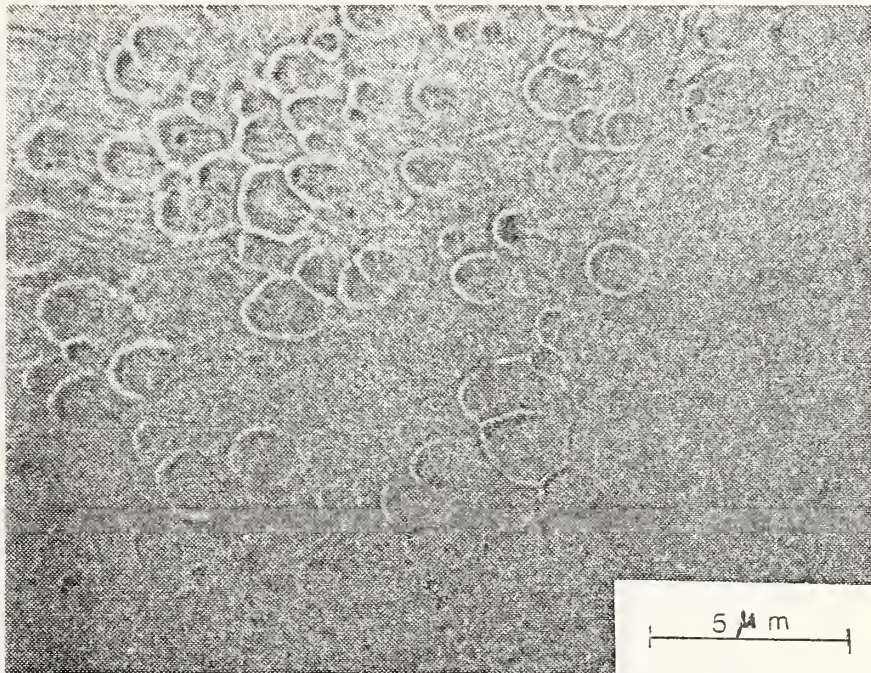


Fig. 5-22. The damaged surface farther out the hole by 3 J laser energy (1 shot)

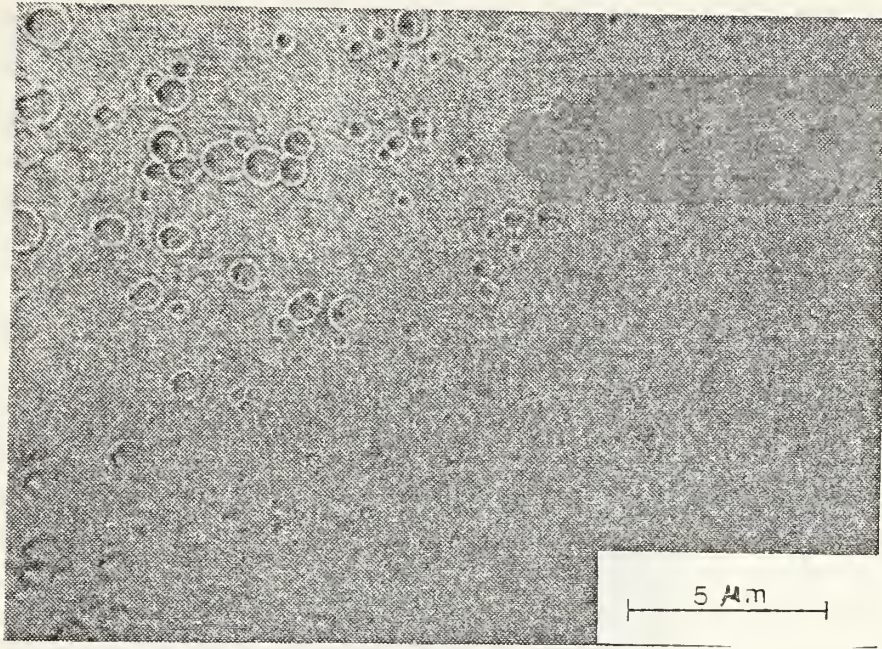


Fig. 5-23. Interface of the damaged and undamaged surface by 3 J laser energy (1 shot)

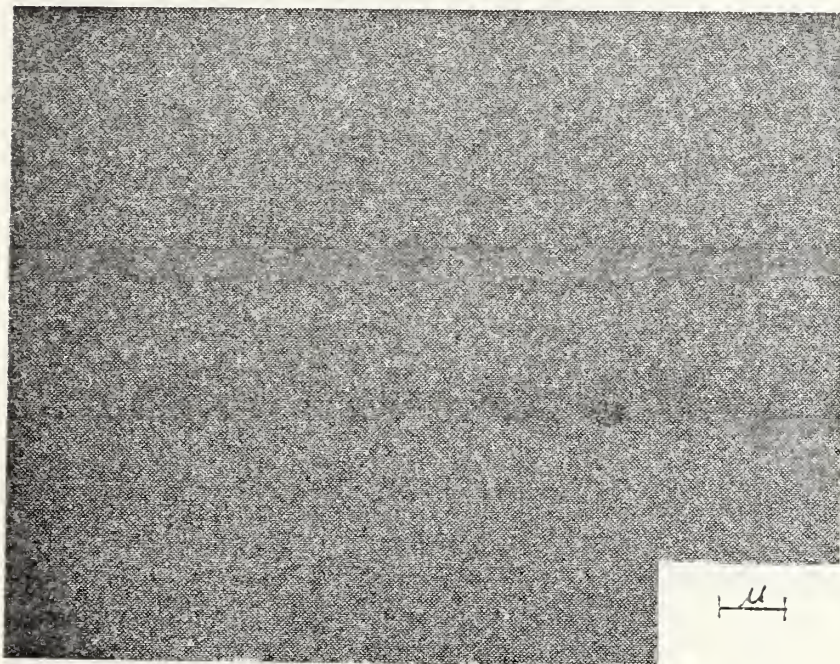


Fig. 5-24. The un-evaporated, polished collector surface

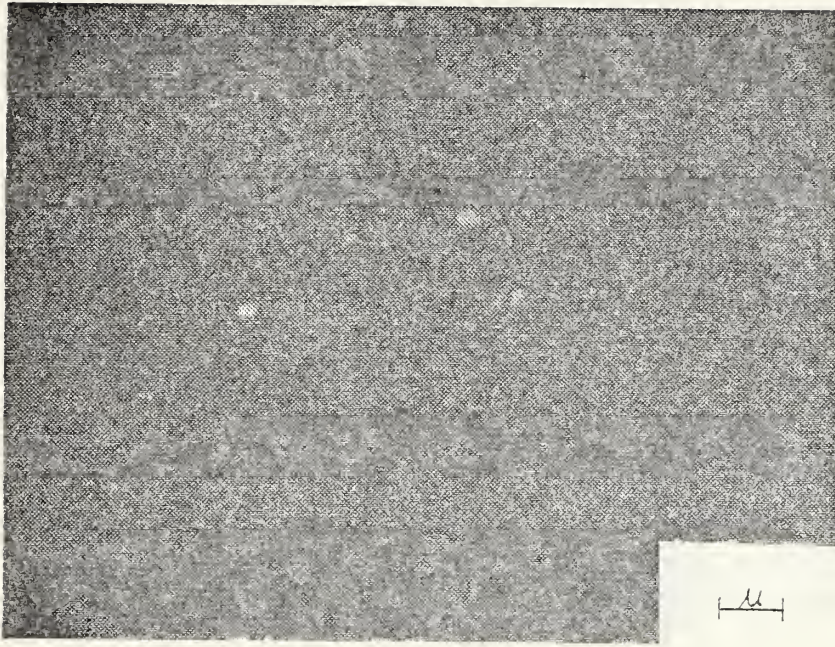


Fig. 5-25. Collection of evaporated materials on the collector plate by 40 shots

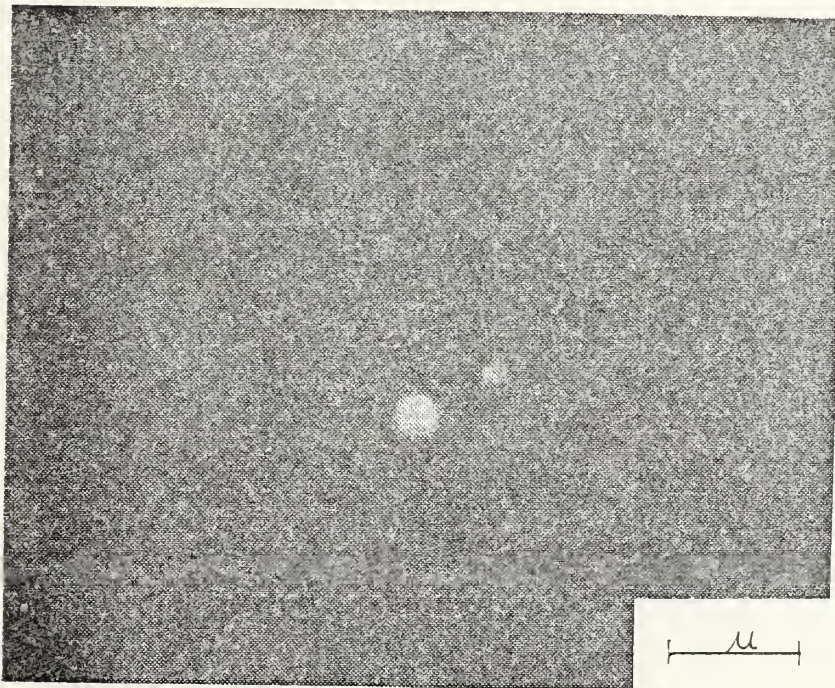


Fig. 5-26. The magnified particles used for calculating the size

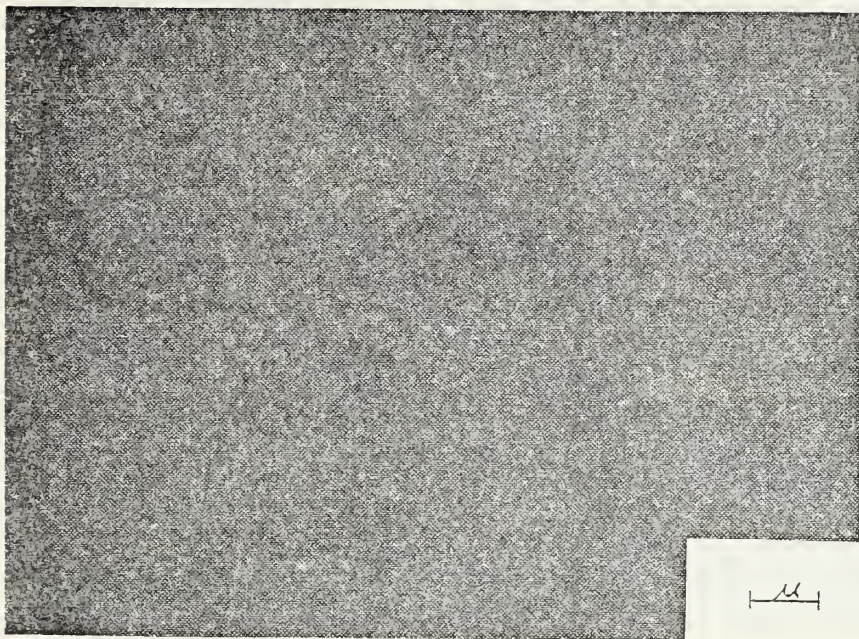


Fig. 5-27. Collection of evaporated materials on the collector plate by 20 shots

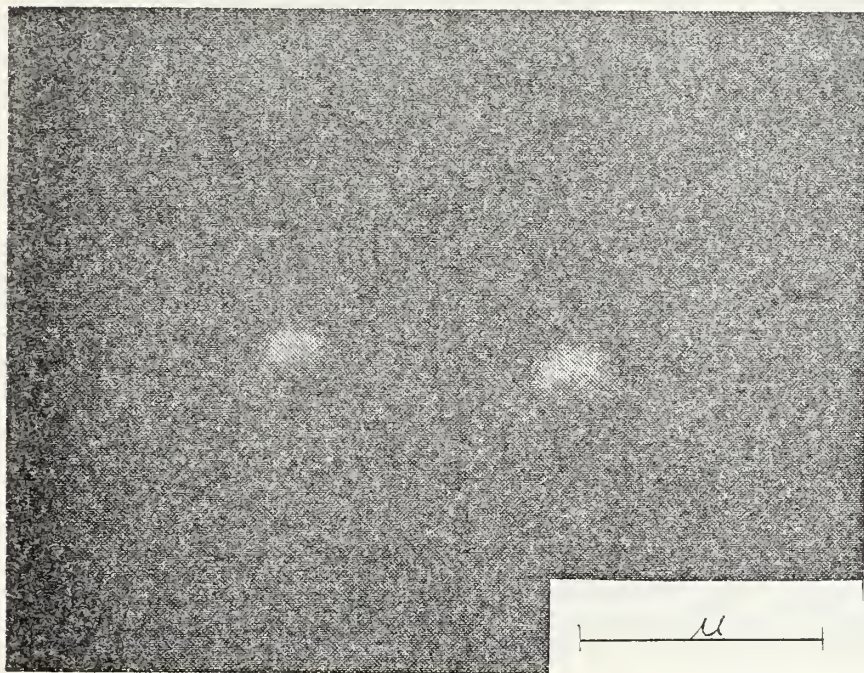


Fig. 5-28. The magnified particles used for calculating the size

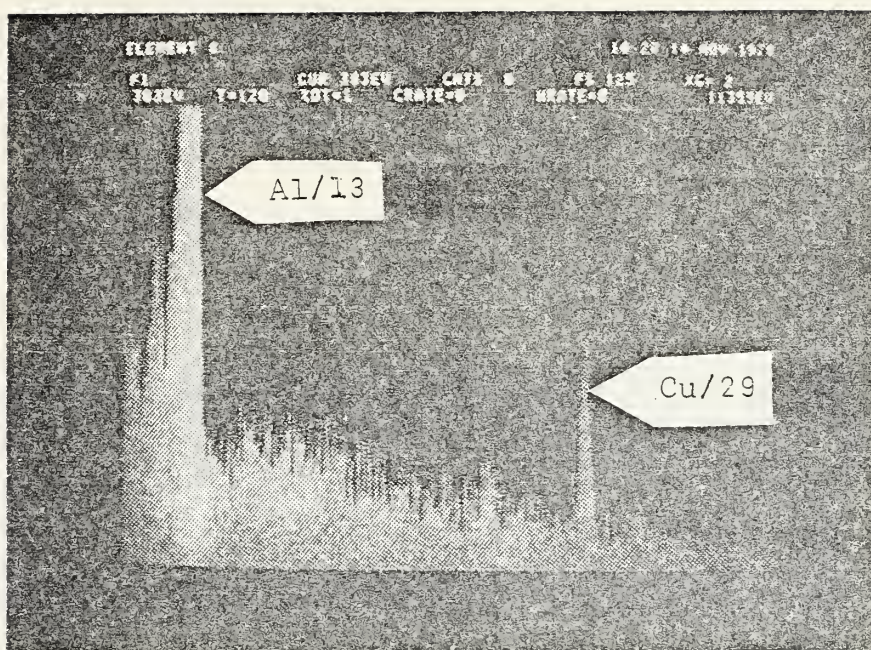


Fig. 5-29. The background spectrum of aluminum collector

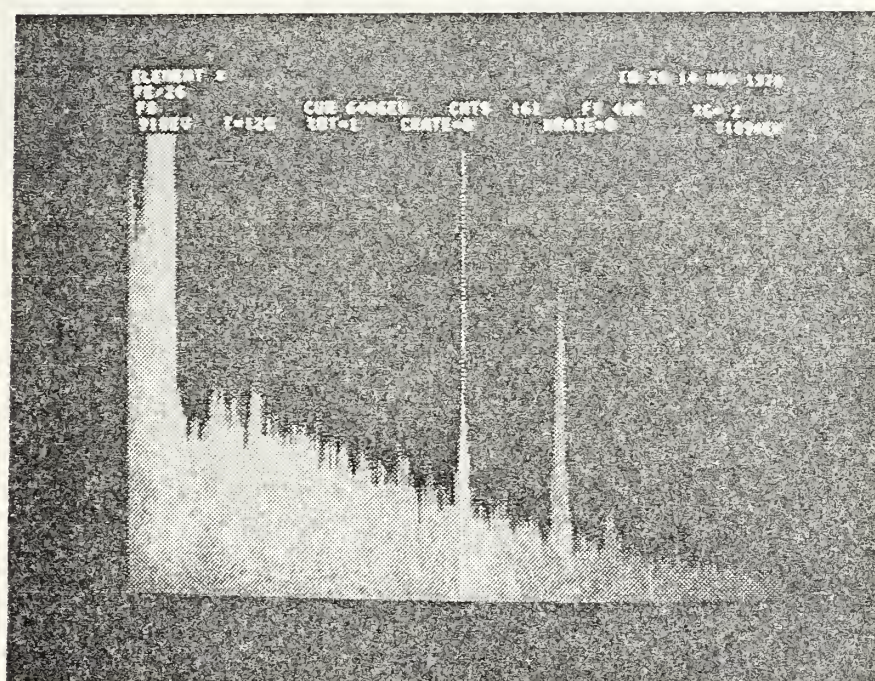


Fig. 5-30. Cursor showed the element Fe/26 deposited on the Aluminum surface after 40 laser shots

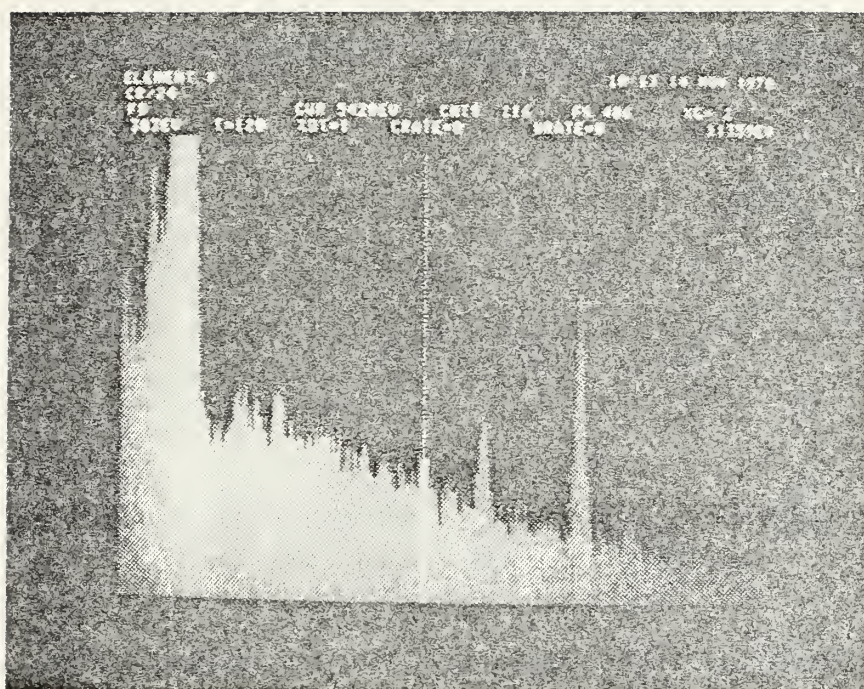


Fig. 5-31. Cursor showed the element $C_r/24$ deposited on the aluminum surface after 40 laser shots

VI. CONCLUSIONS AND RECOMMENDATIONS

Laser-induced evaporation from a stainless steel surface was the laser-target damage mechanism which was studied. It was found that this mechanism depends upon the laser irradiance, the laser pulse shape and the laser pulse width. There were many different models available which dealt with damage mechanisms for various laser irradiances. However, in this experiment, Caruso's model was used because the experimental laser irradiance was in the same range as the irradiance used in the model.

The mass of evaporated material measured in the many shots experiments was approximately one order of magnitude greater than the value calculated according to Caruso's model for a single shot of the same energy. This difference is due to the reduced momentum transfer due to increased screening of the target by the laser produced plasma during a one higher energy shot. Also, with several shots a "softening" of the crystal structure of the target material may occur due to the repetitive heat and shock wave transmitted.

Metallographic studies of the irradiated surface showed the resultant surface breakdown damage. A wave-like pattern of target material surrounded the laser-drilled hole. The scanning electron microscope revealed the presence of an interface between two damage zones which occurred for

laser irradiance on the order of 10^{11} W/cm². For smaller laser irradiances, this interface was not clearly visible. Use of metallographic techniques proved to be very instructive in determining the degree of damage as a function of laser irradiance. Even in a single shot experiment small craters were observed in the outer zone. These small craters are probably caused by small arcs between the plasma and the surface.

The positioning of the collector was determined to be critical in order to collect evaporated target material. Particles of about 3000 Å size were found on a collector plate placed 2 cm from the target. If the collector was located too close to the target, the blowoff materials and pellets would be desorbed by the plasma from the collector. On the other hand, if the collector was located too far away from the target it collected very few evaporated particles due to the rapid expansion of the plasma. Collector surface studies, again using the scanning electron microscope, showed the average separation between particles for a particular magnification. Also, the particles sizes of the evaporated material were observed. Smaller particles existed but did not show up due to the finite limitation of the available magnification.

Mass spectrum analysis of the collector surface was a powerful tool in determining the deposited elements. This analysis was limited to the threshold amount of material

that could be detected. If the mass deposited were too small, it was hidden in the background spectrum. Results of this experiment showed that Fe/26 and Cr/24 were the primary elements composing the particles deposited on the collector surface. These two elements are the primary components of 304 stainless steel.

There is one primary recommendation for improving the analysis of the mass of material evaporated. That is to use different laser irradiances over the range of 10^9 W/cm² to 10^{12} W/cm² based on one large laser pulse. Another recommendation is that carbon stubs should not be used as collectors to capture the evaporated materials. It was found that they result in too much background noise when a specimen is being analyzed with the PGT 1000 x-ray analyzer.

APPENDIX A

THE LASER SYSTEM

The laser used at the Naval Postgraduate School laser-plasma laboratory was the two stage KORAD K-1500 Q-switched neodymium doped glass laser [22]. The general explanation of the neodymium glass laser is given by Maiman [23], and the detailed installation is given by Davis [24]. A block diagram of the basic laser system components is given in figure A-1.

Laser output energy changes by varying the voltages applied to the oscillator and amplifier flashlamps. The energy range of laser output is 0.2 - 15 J. The pulse widths are approximately 25 nanoseconds (FWHM). These small pulse widths are achieved by a pockels cell, Q-switching device mounted between the oscillator and the rear reflector. The unfocused laser beam has an elliptical cross section.

The laser pulse then passes through a thin pane of glass which is called the "beam splitter". The beam splitter reflects a small portion of the output energy onto a magnesium oxide block which in turn reflects it onto a photodiode detector. The detector output signal then connects into a Tektronix 564B storage oscilloscope. This detector signal had been correlated to the total pulse energy measured by a calorimeter over a range from 0 - 15 J.

Laser rod cooling is provided by a cold water recirculating system. The parts of this system are a refrigerator, a water pump, a water filter, two thermometers, a thermostatic temperature control and a reservoir of deionized water. Water is maintained below 20 °C. This insures adequate cooling of the rods with a minimum firing cycle time between laser pulses of five minutes.

There are several power supplies associated with the laser system. A 5-kilovolt maximum variable charged capacitor provides power to the oscillator flash lamp. A 10-kilovolt maximum variable charged capacitor provides power to the amplifier flash lamp. A HV-1565 2000 volt DC power supply energizes the photodiode detector. And finally an integral adjustable shutter control powers the pockels cell device.

For alignment, a CW He-Ne laser is located at the rear of the pockels cell. For safety, a red warning light outside the lab is energized during laser firings. A warning bell also sounds whenever the laser power supplies are charging. The detailed laser operating procedure and general safety precautions are given by Callahan [25].

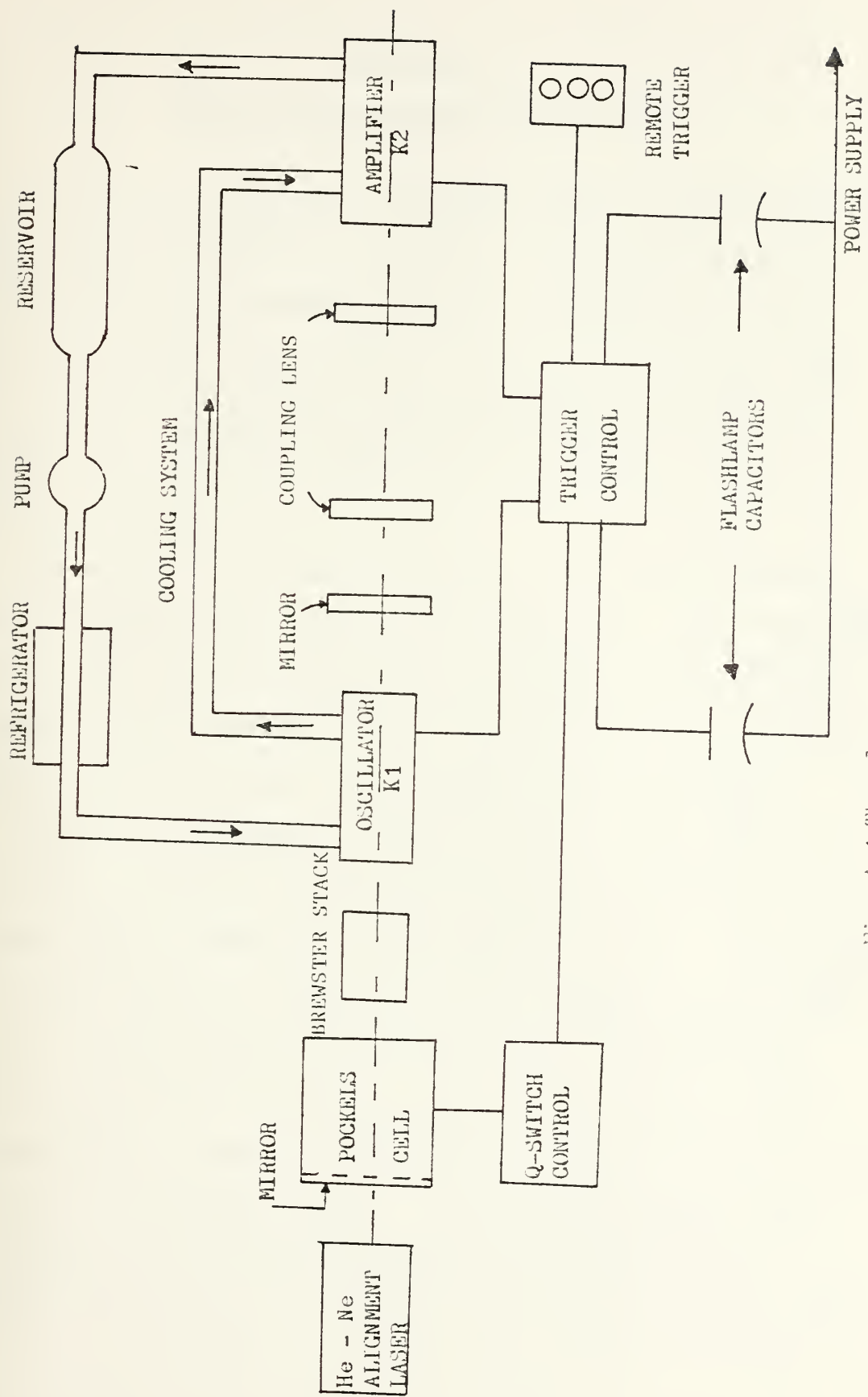


Fig. A-1 The laser system

APPENDIX B

THE SCANNING ELECTRON MICROSCOPE

The scanning electron microscope used in the Mechanical Engineering department at the Naval Postgraduate School is a STEREOSCAN S4-10 scanning electron microscope. The Stereoscan detects and displays information derived from the action of an electron probe scanning the surface of a specimen. The basic operating principles are shown in figure B-1 [27].

The system uses a fine probe of electrons to examine the microtopography of solid bulk specimens. The Stereoscan has a direct reading magnification system which provides a useful range between X20 and X100,000 corresponding to scanned areas of 5 mm to 2 μ m square on the specimen.

The electron probe is formed from a primary beam of electrons, focused to a fine spot on the surface of the specimen by a system of electromagnetic lenses. Low-energy electrons leaving the surface of the specimen due to the action of the electron probe are attracted toward the electron collection system. This system consists of an electrostatic focusing electrode and a scintillator optically coupled to a photomultiplier. Electrons impinging upon the scintillator release photons which travel along a light-guide to the photo-cathode of the photomultiplier.

Signals from the photomultiplier are passed through a head amplifier to a video amplifier and then to the visual display unit, where the amplified signals modulate the brightness of the cathode ray tube beam. This beam scans the tube face of the display unit in synchronism with the scanning of the specimen by the electron probe. The resultant image has a marked three dimensional appearance because contrast is produced by the variation in the number of electrons emitted or reflected from different parts of the specimen. In order to photograph the image, a second display unit is provided on which a camera is mounted.

The specimen is situated in a region of weak magnetic and electrostatic fields and is not subjected to severe heating by the electron beam. The standard specimen stage allows objects of up to 12 mm in diameter and several millimeters thick to be manipulated in any required orientation under observation. The simplified diagram of the column assembly is shown in figure B-2.

The display console contains all of the electronic controls, meters, display units and the operator's desk. The display console is mechanically isolated from the electron optical column.

Power supplies for the system are contained in a rack assembly, sited some distance away from the optical column in order to minimize the effect of magnetic fields on the microscope, and to minimize heat dissipation problems. A photograph of this system is shown in figure B-3.

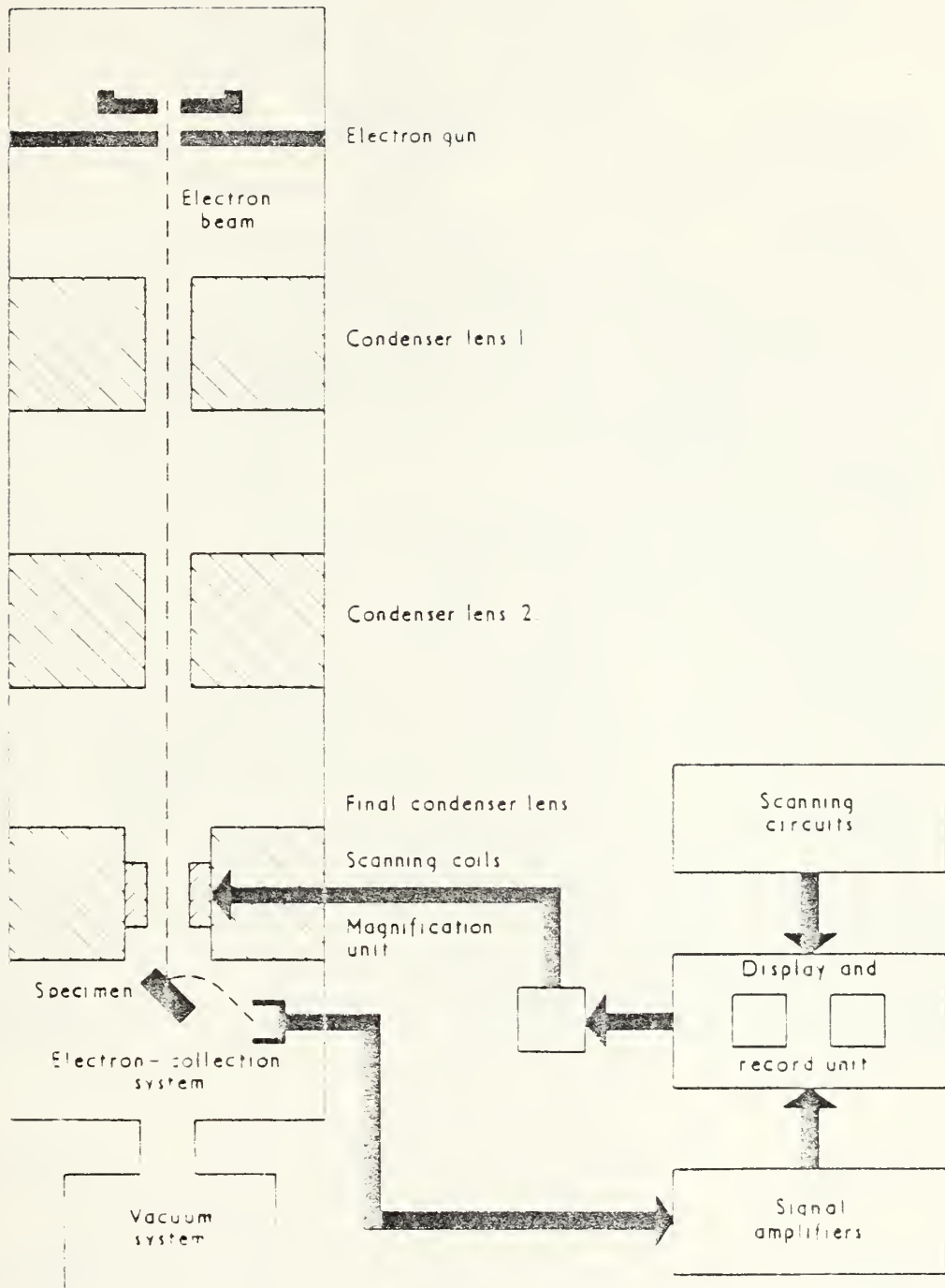


Fig. B-1 Basic principles of operation

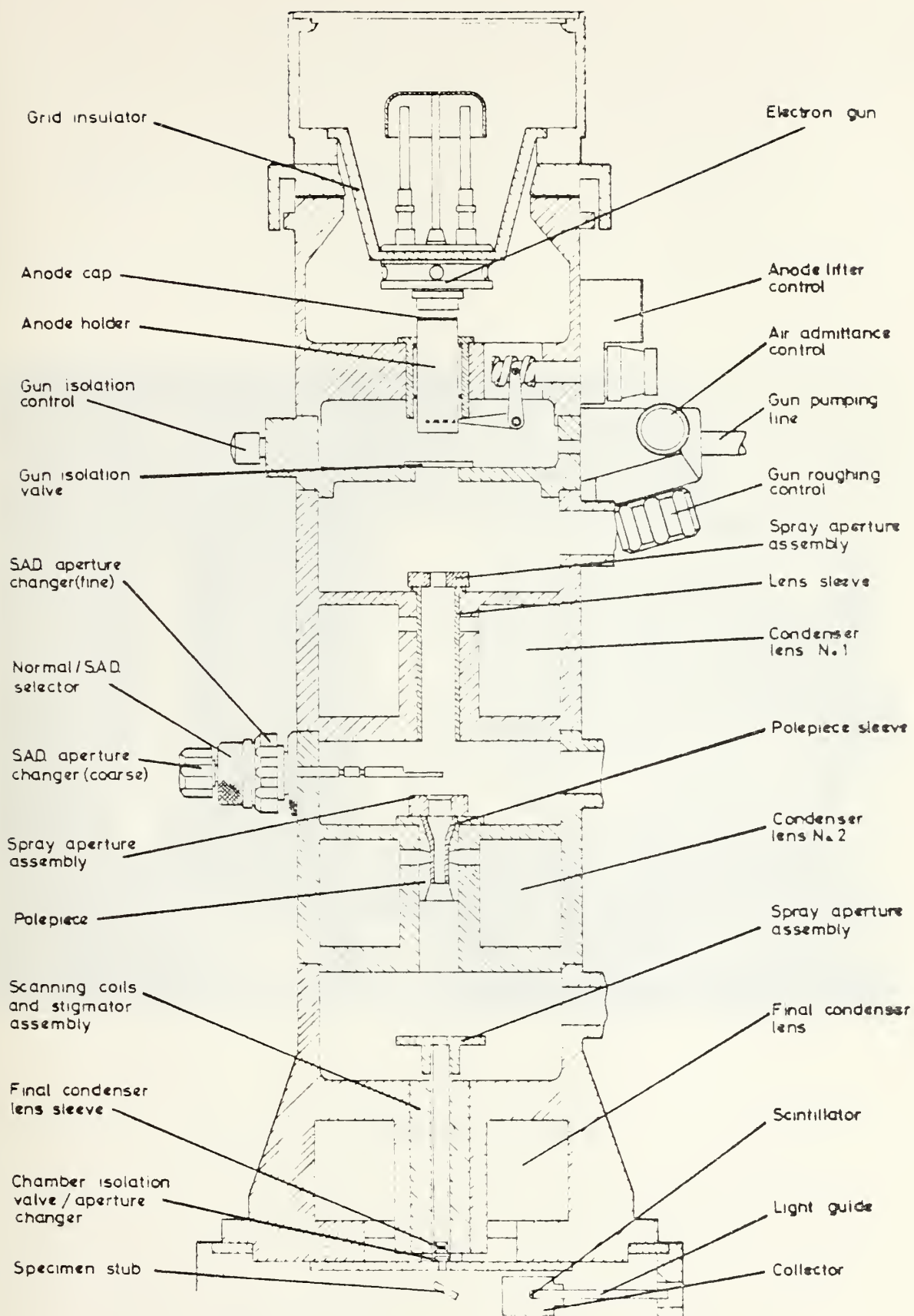


Fig. B-2 Simplified diagram of column assembly

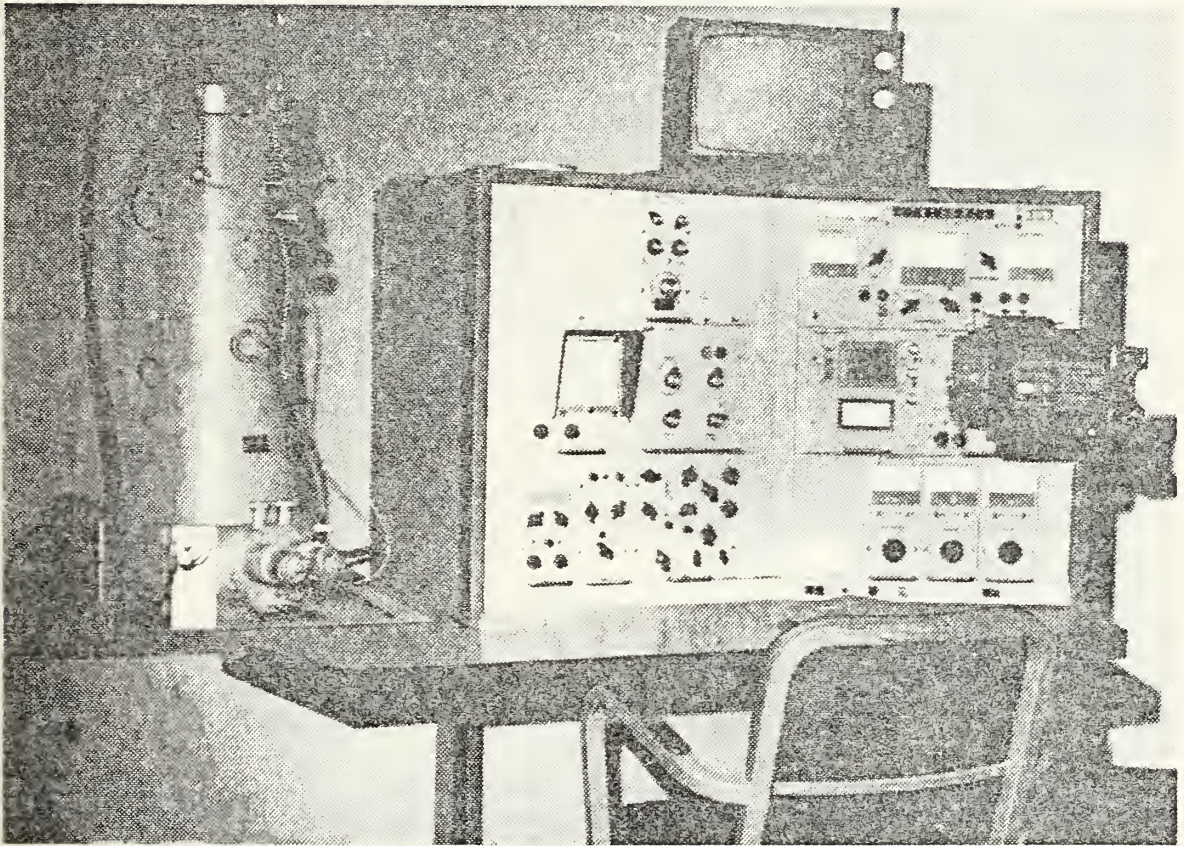


Fig. B-3. Steroscan S4-10 SEM

LIST OF REFERENCES

1. Polk, J.S., Laser Induced Desorption of Gas From Stainless Steel Surfaces. M.S. Thesis, U.S. Naval Postgraduate School, Monterey, California, 1977.
2. Anisimov, S.I., "Evaporation Of A Light-Absorbing Metal", High Temp., V. 6, p. 110, 1968.
3. Ready, J.F., "Mechanism of Electron Emission Produced by a Giant-Pulse Laser", Physical Review, V. 137, No. 2A, P. A620, 1965.
4. Cobb, J.K. and Muray, J.J., "Laser Beam-Induced Electron and Ion Emission from Metal Foils", Brit. J. Appl. Phys., V. 16, P. 271, 1965.
5. Khan, S.H., Richards, F.H. and Walsh, D., "Time Resolution of Laser Induced Electron and Ion Emission", IEEE J. Quantum Electronics, V. 1, P. 359, 1965.
6. Iannuzzi, M. and Williamson, R., "Effects of Absorption of Laser Radiation on Metals", Nuovo Cimento, V. 36, P. 1130, 1965.
7. Stevenson, D.M., "Evaporation and Ionization of Laser-Heated Tungsten", IEEE Proceedings, V. 54, P. 1471, 1966.
8. Berkowitz, J. and Chupka, W.A., "Mass Spectrometric Study of Vapor Ejected from Graphite and Other Solids by Focused Laser Beams", J. Chemical Phys., V. 40, P. 2735, 1964.
9. Schwirzke, F., "Measurements of Spontaneous Magnetic Fields in Laser-Produced Plasma Phenomena", Laser Interaction And Related Plasma Phenomena, Vol. 3, P. 213, Plenum Press, 1974.
10. Harris, T.J., "High-Speed Photographs of Laser-Induced Heating", IBM J. Research Development, V. 7, P. 342, 1963.
11. Bushnell, J.C. and McCloskey, D.J., "Thermoelastic Stress Production in Solids", J. Appl. Physics, V. 39, P. 5541, 1968.

12. Gregg, D.W. and Thomas, S.J., "Momentum Transfer Produced by Focused Laser Giant Pulses", J. of Appl. Physics, V. 37, P. 2787, 1966.
13. Ready, J.F., "Effects Due to Absorption of Laser Radiation", J. of Appl. Physics, V. 36, P. 462, 1965.
14. Carslaw, H.S. and Jaeger, J.C., Conduction of Heat in Solids. Clarendon Press, Oxford, England, P. 110, 1959.
15. Ready, J.F., Effects of High Power Laser Radiation. Academic Press, P. 67-123, 1971.
16. Cohen, M.I., "Melting of a Half-Space Subjected to a Constant Heat Input", J. of the Franklin Institute, V. 283, P. 271, 1967.
17. Landau, H.G., "Heat Conduction in A Melting Solid", Quart. J. Appl. Math. V. 8, P. 81, 1950.
18. Anisimov, S.I., Bonch-Bruevich, A.M., El'yashevich, M.A., Imas, Ya. A., Pavlenko, N.A. and Romanov, G.S., "Effect of Powerful Light Fluxes on Metals", Soviet Physics - Technical Physics, V. 11, P. 945, 1967.
19. Askar'yan, G.A. and Moroz, E.M., "Pressure on Evaporation of Matter in a Radiation Beam", Soviet Physics JETP, V. 16, P. 1638, 1963.
20. Anisimov, S.I., "Vaporization of Metal Absorbing Laser Radiation", Soviet Physics JETP, V. 27, P. 182, 1968.
21. Caruso, A., Bertotti, B. and Giupponi, P., "Ionization and Heating of Solid Material by Means of A Laser Pulse", Il Nuovo Cimento, V. 45B, P. 176, 1966.
22. Union Carbide Electronics, KORAD Laser Systems Instruction Manual for Nd: glass Laser, five volumes, KORAD Dept. Santa Monica, California, 1969.
23. Maiman, T.H., "Optically Pumped Solid State Lasers", Solid State Design, V. 4, P. 17-21, 1963.
24. Davis, L.J., Self-Generated Magnetic Fields Produced by Laser Bombardment of a Solid Target, P. 14-30, M.S. Thesis, U.S. Naval Postgraduate School, Monterey, California, 1971.
25. Callahan, D.J., Laser Plasma Particle Velocities, P. 79-103, M.S. Thesis, U.S. Naval Postgraduate School, Monterey, California, 1976.

26. Varian Associates, Partial Pressure Gauge Mod. 971-0035 and Control Unit Mod. 974-0036 Instruction Manual.
Vacuum Division, Palo Alto, California, 1966.
27. S4-10 Stereoscan Scanning Electron Microscope Manual,
TL 1116-OM-96118-0002, Cambridge Scientific Instruments
Limited.
28. Operator's Manual, The PGT-1000 Disc System, Software
Version 70, August, 1976.
29. Bausch and Lomb, Dynazoom Bench Metallograph Instructions,
Second edition, Second printing, Rochester, New York.

INITIAL DISTRIBUTION LIST

	No. Copies
1. Defense Documentation Center Cameron Station Alexandria, Virginia 22314	2
2. Library, Code 0142 Naval Postgraduate School Monterey, California 93940	2
3. Department Chairman, Code 61Wh Department of Physics and Chemistry Naval Postgraduate School Monterey, California 93940	2
4. Assoc. Prof. F.R. Schwirzke, Code 61Sw Department of Physics and Chemistry Naval Postgraduate School Monterey, California 93940	3
5. Assoc. Prof. R.L. Armstead, Code 61Ar Department of Physics and Chemistry Naval Postgraduate School Monterey, California 93940	2
6. LT. Masami Kawamura 3700 Kamitsuruma Sagamihara-Shi Kanagawa-Ken, JAPAN	1
7. LT. Hwang, Zen-Wen 28 Lane 40 Park 2nd Rd. Yan-Cheng District, Kaohsiung, Taiwan, REPUBLIC OF CHINA	3
8. Chung Shan Institute of Science, Library P.O. Box No. 1, Lung-Tan, Taiwan Republic of China	2

Thesis

H9725

c.1

Hwang

Laser induced evap-
oration from stainless
steel surfaces.

280145

16 MAY 86

30978

Thesis

H9725

c.1

Hwang

Laser induced evap-
oration from stainless
steel surfaces.

280145

Laser induced evaporation from stainless



3 2768 002 13310 0

DUDLEY KNOX LIBRARY

C12